UC Berkeley

UC Berkeley Previously Published Works

Title

The Origin and Evolution of the Normal Type Ia SN 2018aoz with Infant-phase Reddening and Excess Emission

Permalink

https://escholarship.org/uc/item/2fw0677v

Journal

The Astrophysical Journal, 946(1)

ISSN

0004-637X

Authors

Ni, Yuan Qi
Moon, Dae-Sik
Drout, Maria R
et al.

Publication Date

2023-03-01

DOI

10.3847/1538-4357/aca9be

Copyright Information

This work is made available under the terms of a Creative Commons Attribution License, available at https://creativecommons.org/licenses/by/4.0/

Peer reviewed

eScholarship.org Powered by the California Digital Library
University of California

The Astrophysical Journal, 946:7 (29pp), 2023 March 20 https://doi.org/10.3847/1538-4357/aca9be
© 2023. The Author(s). Published by the American Astronomical Society.
OPEN ACCESS

The Origin and Evolution of the Normal Type Ia SN 2018aoz with Infant-phase Reddening and Excess Emission

Yuan Qi Ni[1], Dae-Sik Moon[1], Maria R. Drout[1], Abigail Polin[2,3], David J. Sand[4], Santiago González-Gaitán[5], Sang Chul Kim[6,7], Youngdae Lee[6,8], Hong Soo Park[4,6,7], D. Andrew Howell[9,10], Peter E. Nugent[11,12], Anthony L. Piro[2], Peter J. Brown[13,14], Lluís Galbany[15,16], Jamison Burke[9,10], Daichi Hiramatsu[9,10,17,18], Griffin Hosseinzadeh[4], Stefano Valenti[19], Niloufar Afsariardchi[1], Jennifer E. Andrews[4], John Antoniadis[20,21,22], Rachael L. Beaton[2,23,37,38], K. Azalee Bostroem[24], Raymond G. Carlberg[1], S. Bradley Cenko[25,26], Sang-Mok Cha[6,27], Yize Dong[19], Avishay Gal-Yam[28], Joshua Haislip[29], Thomas W.-S. Holoien[2], Sean D. Johnson[23], Vladimir Kouprianov[29,30], Yongseok Lee[6,27], Christopher D. Matzner[1], Nidia Morrell[31], Curtis McCully[9,10], Giuliano Pignata[32,33], Daniel E. Reichart[29], Jeffrey Rich[2], Stuart D. Ryder[34,35], Nathan Smith[4], Samuel Wyatt[4], and Sheng Yang[36]

[1] David A. Dunlap Department of Astronomy and Astrophysics, University of Toronto, 50 St George Street, Toronto, ON M5S 3H4, Canada
chris.ni@mail.utoronto.ca
[2] The Observatories of the Carnegie Institution for Science, 813 Santa Barbara Street, Pasadena, CA 91101, USA
[3] TAPIR, Walter Burke Institute for Theoretical Physics, Caltech, 1200 East California Boulevard, Pasadena, CA 91125, USA
[4] Department of Astronomy/Steward Observatory, University of Arizona, 933 North Cherry Avenue, Rm. N204, Tucson, AZ 85721-0065, USA
[5] CENTRA, Instituto Superior Técnico, Universidade de Lisboa, Avenida Rovisco Pais, 1049-001 Lisboa, Portugal
[6] Korea Astronomy and Space Science Institute, 776 Daedeokdae-ro, Yuseong-gu, Daejeon 34055, Republic of Korea
[7] Korea University of Science and Technology (UST), 217 Gajeong-ro, Yuseong-gu, Daejeon 34113, Republic of Korea
[8] Department of Astronomy and Space Science, Chungnam National University, 99 Daehak-ro, Yuseong-gu, Daejeon 34134, Republic of Korea
[9] Department of Physics, University of California, Santa Barbara, CA 93106-9530, USA
[10] Las Cumbres Observatory, 6740 Cortona Drive, Suite 102, Goleta, CA 93117-5575, USA
[11] Lawrence Berkeley National Laboratory, 1 Cyclotron Road, 1 Berkeley, CA 94720-8197, USA
[12] Department of Physics and Astronomy, University of California Berkeley, Berkeley, CA 94720 USA
[13] Department of Physics and Astronomy, Texas A&M University, 4242 TAMU, College Station, TX 77843-4242, USA
[14] George P. and Cynthia Woods Mitchell Institute for Fundamental Physics & Astronomy, College Station, TX 77843, USA
[15] Institute of Space Sciences (ICE, CSIC), Campus UAB, Carrer de Can Magrans, s/n, E-08193 Barcelona, Spain
[16] Institut d'Estudis Espacials de Catalunya (IEEC), E-08034 Barcelona, Spain
[17] Center for Astrophysics | Harvard & Smithsonian, 60 Garden Street, Cambridge, MA 02138-1516, USA
[18] The NSF AI Institute for Artificial Intelligence and Fundamental Interactions, Cambridge, MA 02139, USA
[19] Department of Physics and Astronomy, University of California Davis, 1 Shields Avenue, Davis, CA 95616-5270, USA
[20] Institute of Astrophysics, FORTH, Department of Physics, University of Crete, Voutes, University Campus, GR-71003 Heraklion, Greece
[21] Max-Planck Institut für Radioastronomie, Auf dem Hügel 69, 53121 Bonn, Germany
[22] Argelander Institut für Astronomie, Auf dem Hügel 71, 53121 Bonn, Germany
[23] Department of Astrophysical Sciences, Princeton University, 4 Ivy Lane, Princeton, NJ 08544, USA
[24] DIRAC Institute, Department of Astronomy, University of Washington, 3910 15th Avenue NE, Seattle, WA 98195, USA
[25] Astrophysics Science Division, NASA Goddard Space Flight Center, MC 661, Greenbelt, MD 20771, USA
[26] Joint Space-Science Institute, University of Maryland, College Park, MD 20742, USA
[27] School of Space Research, Kyunghee University, 1732 Deogyeong-daero, Giheung-gu, Yongin-si, Gyeonggi-do 17104, Republic of Korea
[28] Department of Particle Physics and Astrophysics, Weizmann Institute of Science, 234 Herzl Street, Rehovot 76100, Israel
[29] Department of Physics and Astronomy, University of North Carolina at Chapel Hill, 120 E. Cameron Avenue, Chapel Hill, NC 27599-3255, USA
[30] Central (Pulkovo) Observatory of Russian Academy of Sciences, 196140 Pulkovskoye Avenue 65/1, Saint Petersburg, Russia
[31] Las Campanas Observatory, Carnegie Observatories, Casilla 601, La Serena, Chile
[32] Departamento de Ciencias Fisicas, Universidad Andres Bello, Avenida República 252, Santiago, 8370134, Chile
[33] Millennium Institute of Astrophysics (MAS), Nuncio Monseñor Sotero Sanz 100, Providencia, Santiago, Chile
[34] School of Mathematical and Physical Sciences, Macquarie University, 105 Delhi Road, North Ryde NSW 2109, Australia
[35] Macquarie University Research Centre for Astronomy, Astrophysics & Astrophotonics, Sydney NSW 2109, Australia
[36] The Oskar Klein Centre, Department of Astronomy, Stockholm University, AlbaNova SE-10691 Stockholm, Sweden
Received 2022 June 24; revised 2022 December 2; accepted 2022 December 5; published 2023 March 21

Abstract

SN 2018aoz is a Type Ia SN with a *B*-band plateau and excess emission in infant-phase light curves $\lesssim$1 day after the first light, evidencing an over-density of surface iron-peak elements as shown in our previous study. Here, we advance the constraints on the nature and origin of SN 2018aoz based on its evolution until the nebular phase. Near-peak spectroscopic features show that the SN is intermediate between two subtypes of normal Type Ia: core normal and broad line. The excess emission may be attributable to the radioactive decay of surface iron-peak elements as well as the interaction of ejecta with either the binary companion or a small torus of circumstellar

[37] Hubble Fellow.
[38] Carnegie-Princeton Fellow.

Original content from this work may be used under the terms of the Creative Commons Attribution 4.0 licence. Any further distribution of this work must maintain attribution to the author(s) and the title of the work, journal citation and DOI.

material. Nebular-phase limits on Hα and He I favor a white dwarf companion, consistent with the small companion size constrained by the low early SN luminosity, while the absence of [O I] and He I disfavors a violent merger of the progenitor. Of the two main explosion mechanisms proposed to explain the distribution of surface iron-peak elements in SN 2018aoz, the asymmetric Chandrasekhar-mass explosion is less consistent with the progenitor constraints and the observed blueshifts of nebular-phase [Fe II] and [Ni II]. The helium-shell double-detonation explosion is compatible with the observed lack of C spectral features, but current 1D models are incompatible with the infant-phase excess emission, $B_{\rm max}-V_{\rm max}$ color, and weak strength of nebular-phase [Ca II]. Although the explosion processes of SN 2018aoz still need to be more precisely understood, the same processes could produce a significant fraction of Type Ia SNe that appear to be normal after $\sim$1 day.

Key words: Binary stars – Supernovae – Type Ia supernovae – White dwarf stars – Transient sources – Time domain astronomy

Supporting material: machine-readable table

1. Introduction

Type Ia SNe are thermonuclear explosions of carbon and oxygen white dwarfs (C+O WDs; Nugent et al. 2011). They are the main source of iron-peak elements in the universe and crucial for measuring extragalactic distances, leading to the discovery of the accelerated cosmological expansion and dark energy (Riess et al. 1998; Perlmutter et al. 1999). Despite their fundamental importance, the explosion mechanisms and progenitor systems of Type Ia SNe remain a matter of extensive debate (Maoz et al. 2014). Understanding the origins of Type Ia SNe, particularly of the *normal* events comprising $\sim$70% of their population (Blondin et al. 2012), will not only clarify the end states of stellar evolution but will be essential for improving cosmological distance measurements (e.g., Wang et al. 2013; Zhang et al. 2021).

There is a broad consensus that Type Ia SNe explode as a result of mass transfer in binary progenitor systems. However, uncertainty remains about whether the binary companion involved in normal Type Ia SN explosions is an evolved nondegenerate star (*single-degenerate scenario*; Whelan & Iben 1973) or another WD (*double-degenerate scenario*; Iben & Tutukov 1984). In the latter case, it is unclear whether the explosion would be triggered during WD-WD accretion (Guillochon et al. 2010; Pakmor et al. 2013), or in a complete merger (Pakmor et al. 2012), or head-on collision of the two WDs (Kushnir et al. 2013). The *core-degenerate scenario* is a third hypothesis where Type Ia SNe result from mergers of WDs with the cores of asymptotic giant branch stars (Aznar-Siguan et al. 2015).

The mechanisms responsible for triggering normal Type Ia SN explosions are also unclear. Normal Type Ia SNe have long been theorized to be ignited by nuclear burning in the core of a WD when accretion or merger causes its mass to reach the critical Chandrasekhar limit ($\sim$1.4 $M_{\odot}$; Mazzali et al. 2007). Alternatively, recent theoretical studies have suggested that the detonation of a thin helium layer on the surface of a sub-Chandrasekhar-mass WD can subsequently ignite carbon in the core, producing normal Type Ia SNe via *helium-shell double-detonation* (He-shell DDet; Polin et al. 2019; Townsley et al. 2019; Magee et al. 2021; Shen et al. 2021a). One scenario that has been thought to result in a He-shell DDet is the detonation of He-rich material on the WD surface during a double-degenerate accretion process, called *dynamically driven double-degenerate double-detonation* (or D^6), recently supported by the identification of hyper-velocity Galactic WDs interpreted to be survivors of the scenario (Shen et al. 2018; Bauer et al. 2021).

Multiple explosion and progenitor channels may ultimately contribute to the observed population of Type Ia SNe. In particular, the normal events consist of two spectroscopically distinct subtypes (Parrent et al. 2014): *core normal/normal velocity* (CN/NV); and *broad line/high velocity* (BL/HV). Events from the two subtypes are nearly indistinguishable in their light curves, with similar peak brightness and decline rate, but differ in their observed spectroscopic features (Branch et al. 2006) and ejecta velocities (Wang et al. 2009). Different explosion mechanisms—such as Chandrasekhar- and sub-Chandrasekhar-mass explosions (e.g., Polin et al. 2019; Li et al. 2021)—have been suggested to explain the differences between the two subtypes. Alternatively, unified origins for the observed spectroscopic diversity in normal events have also been proposed, usually involving an asymmetric explosion mechanism (e.g., Maeda et al. 2010c).

Early (e.g., $\lesssim$5 days post-explosion) light curves of Type Ia SNe can shed light on their origins by providing critical constraints on the binary companion, circumstellar material (CSM) from accretion or merger, and the distribution of elements in the outer ejecta. Theoretical models have predicted that the collision between the SN ejecta and a binary companion (Kasen 2010) or CSM (Piro & Morozova 2016) can shock heat the ejecta, producing blue excess emission. Multiple explosion processes, including subsonic mixing (Reinecke et al. 2002) and detonation of surface helium (Maeda et al. 2018; Polin et al. 2019; Magee et al. 2021), have also been predicted to lead to over-densities of radioactive iron-peak (Fe-peak) elements, including ^{56}Ni, ^{52}Fe, and ^{48}Cr, in the shallow layers of the ejecta, leading to the excess emission and short-lived color evolution associated with Fe spectroscopic features. Such color and light-curve features occurring within $\sim$5 days have been reported in many Type Ia SNe (Marion et al. 2016; Hosseinzadeh et al. 2017, 2022; Jiang et al. 2017, 2018; Miller et al. 2018, 2020a; Stritzinger et al. 2018; De et al. 2019; Li et al. 2019; Shappee et al. 2019; Dimitriadis et al. 2019; Bulla et al. 2020; Tucker et al. 2021; Ni et al. 2022; Deckers et al. 2022), though there have been recent debates about their interpretation in some normal events (e.g., Sand et al. 2018b; Shappee et al. 2018; Ashall et al. 2022). However, for the vast majority of Type Ia SNe observed between 1 and 5 days, their light curves match simple power-law profiles in this phase (Bloom et al. 2012; Foley et al. 2012; Olling et al. 2015; Cartier et al. 2017; Holmbo et al. 2019; Yao et al. 2019; Moon et al. 2021). Such power-law evolution is consistent with an origin that has both (1) a small nondegenerate or WD companion and (2) leads to a ^{56}Ni distribution in the ejecta

that is largely centrally concentrated and monotonically declining toward the surface.

Another way to critically constrain the explosion mechanism and progenitor system is to investigate spectral features of Type Ia SNe from the so-called *nebular phase* of $\gtrsim$200 days since the *B*-band maximum. Differences in the Doppler shifts of [Fe II] and [Ni II] emission lines observed in normal Type Ia SNe have been attributed to the viewing angle effects of asymmetric explosion mechanisms (Maeda et al. 2010b, 2010c; Maguire et al. 2018; Li et al. 2021). Meanwhile, strong [Ca II] emission has been associated with incomplete nuclear burning in the core of sub-Chandrasekhar-mass explosions (Polin et al. 2021; Siebert et al. 2020). For the progenitor, the presence of Hα and He I emission by stripped/ablated H and He from a nondegenerate companion has been predicted by several recent studies as evidence supporting single degeneracy (Mattila et al. 2005; Botyanszki et al. 2018; Dessart et al. 2020). Such Hα emission has been observed in the nebular-phase spectra of a few peculiar events (e.g., Kollmeier et al. 2019), indicating that they may be from single-degenerate progenitors. However, systematic searches for H and He emission in the nebular-phase spectra of >100 Type Ia SNe have failed to find such emission in most of them ($\gtrsim$90%), disfavoring the single-degenerate scenario as the primary contributor to the Type Ia SN population (Mattila et al. 2005; Leonard 2007; Shappee et al. 2013; Maguire et al. 2016; Tucker et al. 2020). However, a systematic search for H and He emission in the nebular-phase spectra of 110 Type Ia SNe has failed to find such emission in most of them ($\gtrsim$90%), disfavoring the single-degenerate scenario as the primary contributor to the Type Ia SN population (Tucker et al. 2020). [O I] emission has also been detected in the nebular-phase spectra of two peculiar events and interpreted to be evidence for the presence of swept-up unburned O from a double-degenerate merger (Kromer et al. 2013; Taubenberger et al. 2013). The identification of such [O I] emission has yet to be made for normal events.

SN 2018aoz is a recent normal Type Ia SN detected 1.0 hr after its estimated epoch of the first light[39] (MJD 58206.00), the earliest detection for a Type Ia SN ever made so far (Ni et al. 2022, Paper I hereafter). Photometric and spectroscopic observations were obtained over the ensuing period of ~450 days, including light curves of the first 12 hr from the very low brightness of −10.5 absolute *AB* magnitude. This data set provides the unique opportunity to study the entire evolution of a normal Type Ia SN from 1 hr after the first light to the nebular phase. In Paper I, we presented the discovery of two new infant-phase features of Type Ia SN evolution during the first 1.0–12.4 hr: a brief *B*-band plateau—which disappears after ~0.5 day—and simultaneous excess emission in the *V* and *i* bands. The subsequent evolution of SN 2018aoz until ~110 days is consistent with that of typical normal Type Ia SNe, with a power-law light-curve rise, peak *B*-band absolute magnitude of −19.32 mag, and $\Delta M_{15}(B)$ of 1.12 mag. The two infant-phase features result in a rapid reddening of the $B-V$ color, which has been associated with line-blanket absorption by an over-density of Fe-peak elements in the outer 1% of the SN-ejected mass (Paper I). This has important implications for the normal Type Ia SN explosion mechanism, as such an ejecta composition is primarily predicted by asymmetric Chandrasekhar-mass explosions and He-shell DDets.

Although SN 2018aoz has provided critical information on the distribution of surface Fe-peak elements, its evolution to the nebular phase has yet to be explored and additional insights into its origin can be gained by (1) placing constraints on the nature of its companion star, (2) examining the physical implications of a range of possible power sources for the infant-phase excess emission, and (3) assessing its precise subtype among normal Type Ia SNe. In this paper, we present new photometric and spectroscopic observations of the nebular phase of SN 2018aoz in Section 2, as well as detailed modeling and interpretation of key features to understand its origin and evolution as follows. In Section 3, we describe the evolution of the light curves and spectra of SN 2018aoz, including comparisons of them to those of other Type Ia SNe in order to establish its spectroscopic subtype. We assess the range of companion stars that are compatible with the luminosity of the observed early light curve in Section 4. Sections 5–7 describe our modeling of the infant-phase excess emission, provide analyses of the nebular-phase observations, and comparisons to the predictions of He-shell DDet simulations, respectively. In Section 8, we discuss the implications of our results for the progenitor system and explosion mechanism of SN 2018aoz, the nature of its infant-phase excess emission, and the origins of normal Type Ia SNe. We summarize our results and conclude in Section 9.

2. Observations and Data

SN 2018aoz was identified by both the KMTNet Supernova Program (KSP; Moon et al. 2016, 2021; Afsariardchi et al. 2019; Lee et al. 2022) and Distance Less Than 40 Mpc Survey (DLT40; Tartaglia et al. 2018). The earliest detection of the SN with a signal-to-noise ratio (S/N) > 3 was made by KSP in the *B* band at $00^{h}54^{m}$ on 2018 March 29 UT, or MJD 58206.0378. DLT40 detected the source 1.1 days later in the *r* band and reported the discovery of SN 2018aoz at $07^{h}25^{m}$ on 2018 April 2 UT (Sand et al. 2018a). The first spectrum obtained by the Las Cumbres Observatory (Brown et al. 2013) at $09^{h}25^{m}$ on 2018 April 2 UT subsequently classified the source as a Type Ia SN(Hosseinzadeh et al. 2018). The discovery triggered an extensive campaign of ground- and space-based photometric observations as well as spectroscopic follow-up, obtaining observations in the UV to near-IR (NIR) wave bands. The early observations of SN 2018aoz obtained ~110 days since the first light were presented in Paper I. Here, we present additional KSP photometry continuing from >250 days since the first light, covering the nebular phase (Section 2.1), as well as new nebular-phase spectroscopy of the SN (Section 2.2).

2.1. Nebular-phase Photometry

We used the three 1.6 m telescopes of the Korea Microlensing Telescope Network (KMTNet; Kim et al. 2016) in Chile, South Africa, and Australia to conduct photometric observations of SN 2018aoz during its nebular phase, >200 days since the *B*-band maximum. Each telescope of the network is equipped with an identical wide-field CCD camera with 4 $\deg^2$ field of view and multiple filters in the visible band. Between 2018 December and 2019 June, we conducted high-cadence monitoring of a $2^\circ \times 2^\circ$ field containing the source, obtaining

[39] First light refers to the epoch when photons first emerge from the ejecta, which may follow the explosion by a few hours to days in Type Ia SNe, depending on the photon diffusion process (Piro & Nakar 2013, 2014). In SN 2018aoz, the epoch of explosion is estimated to be MJD 58205.6 ± 0.7 based on the observed evolution of photospheric velocity (Paper I).

~500 images of the field with 60 s exposure times at a mean cadence of ~9 hr in each of the *BVI* bands. The *B*, *V*, and *I* bands are observed nearly simultaneously at each epoch with a time difference of ~2 minutes between adjacent filters. The typical limiting magnitude for a point source in these images is 21–22 mag at an S/N of 3. Note that the source was not observed between July and November due to its proximity to the Sun.

We performed point-spread function (PSF) photometry of SN 2018aoz using the SuperNova Analysis Package (SNAP; Ni 2022),[40] a custom python-based pipeline for supernova photometry and analysis. A local PSF was obtained by fitting a Moffat function (Moffat 1969; Trujillo et al. 2001) to nearby reference stars and simultaneously fitting sky background emission with a first-order polynomial function. The fluxes of SN 2018aoz in the *B* and *V* bands were obtained by fitting the local PSF near the source location. Paper I reported the presence of a faint background source ~0.″8 northwest of the position of SN 2018aoz with apparent magnitudes of 24.90 ± 0.27, 24.02 ± 0.20, and 22.39 ± 0.08 mag in the *BVi* bands, respectively, which mainly affect the *i* band. Therefore, we measure the *i*-band SN flux in the nebular phase by using a Kron aperture containing both sources and subtracting the known flux of the background source from the combined flux in the aperture. Since the brightness of the background source is significantly fainter than that of the 1σ noise level in the *B*- and *V*-band images ($\lesssim$23.4 mag) and the SN at any epoch (<22.0 mag for the *B* band and <22.1 mag for the *V* band), it is incapable of meaningfully affecting the PSF photometry of the SN in those bands.

Photometric flux calibration was performed against 6–9 standard reference stars within 10′ of the source from the AAVSO Photometric All-Sky Survey[41] database whose apparent magnitudes are in the range of 15–16 mag. The observations in the *BVI* KMTNet filters were calibrated against reference stars in the nearest AAVSO filters (Johnson *BV*, and Sloan *i*′; or *BVi*). For the AAVSO reference stars, their KSP *BVI* instrumental magnitudes were transformed to standard *BVi* filters using the equations from Park et al. (2017). For the SN, since its nebular-phase spectra are significantly different from the AAVSO standard stars used to derive the Park et al. (2017) equations, we applied linearly interpolated spectrophotometric (S) corrections (Stritzinger et al. 2002). These are photometric corrections between the instrument and standard filters derived by performing synthetic photometry on spectra obtained at approximately the same epoch. The calibrated and S-corrected nebular-phase photometry is presented in Table 1 and shown in Figure 1.

2.2. Nebular-phase Spectroscopy

We obtained four low-resolution nebular-phase optical spectra of SN 2018aoz at 259.4, 277.3, 296.4, and 382.5 days since the *B*-band maximum with a combination of the Gemini Multi-Object Spectrograph (GMOS; Hook et al. 2004) on Gemini-South, the Low Resolution Imaging Spectrometer (LRIS; Oke et al. 1995) on Keck, and the Low Dispersion Survey Spectrograph-3 (LDSS-3; Allington-Smith et al. 1994) on Magellan-Clay. The spectroscopic observations are summarized in Table 2.

[40] https://github.com/niyuanqi/SNAP
[41] https://www.aavso.org/apass

Table 1
Nebular-phase Magnitudes of SN 2018aoz

Time (MJD)	Band	Magnitude[a] (mag)	Error (mag)
58471.68652	*B*	19.195	0.065
58471.68830	*B*	19.267	0.061
58471.68979	*V*	19.562	0.128
58471.69130	*i*	19.430	0.177
58472.68728	*B*	19.302	0.074
58472.68862	*V*	19.374	0.092
58472.69015	*i*	19.585	0.285
58473.68083	*B*	19.346	0.082
58473.68233	*V*	19.554	0.096
58473.68382	*i*	19.420	0.177

Notes. Sample of the observed magnitudes of SN 2018aoz during its nebular phase. The entire observed magnitudes of SN 2018aoz are available in the electronic edition.
[a] The *BV*-band magnitudes are in the Vega system, while the *i*-band magnitudes are in the AB system (see the text).
(This table is available in its entirety in machine-readable form.)

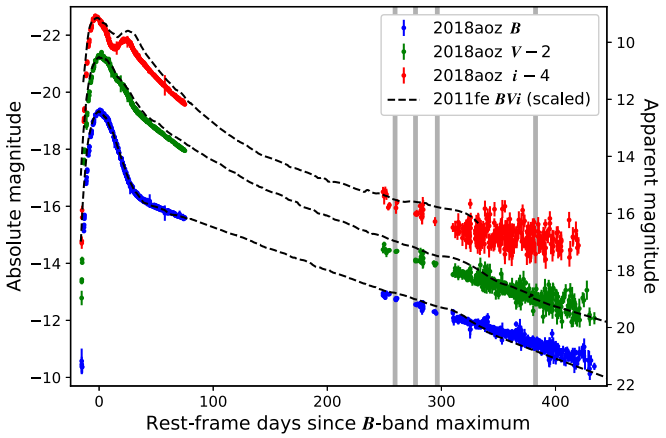

Figure 1. The dereddened *BVi*-band light curves of SN 2018aoz (colored circles) relative to the epoch of the *B*-band maximum light in the rest frame covering its nebular phase compared to those of SN 2011fe (dashed lines; Munari et al. 2013; Tsvetkov et al. 2013), which have been scaled so that they match the M_B and $\Delta M_{15}(B)$ values of SN 2018aoz. The error bars represent the 1σ uncertainty level in this figure and all of the following. The vertical gray lines mark the four epochs with nebular-phase spectroscopy (see Table 2 and Figure 2).

The spectrum from the Magellan Telescope was reduced using standard tasks within IRAF. Bias and flat-field corrections were performed on the two-dimensional frames, one-dimensional spectra were extracted, and wavelength calibration was performed using calibration lamps taken immediately after target exposures. Flux calibration and telluric corrections were performed with a set of custom IDL scripts (Matheson et al. 2008; Blondin et al. 2012) using spectrophotometric standards observed on the same night. The GMOS spectra were reduced in a similar manner, but using the custom `gmos` suite of IRAF tasks. The initial flux calibration for GMOS spectra was performed using the IRAF tasks `standard` and `calibrate`, and final scaling was performed based on matching to the observed *V*-band photometry from the same epochs. The Keck-LRIS spectrum was reduced using LPipe, a fully automated IDL pipeline for the LRIS (Perley 2019). The reduced and dereddened nebular-phase spectra are shown in Figure 2.

Table 2
Nebular-phase Spectroscopy of SN 2018aoz

Date (UT)	Phase	Telescope	Instrument	R	Wavelength (Å)
2018 Dec 30.28	+259.4	Gemini-S	GMOS	1690	4050–10,000
2019 Jan 17.31	+277.3	Gemini-S	GMOS	1690	5000–10,000
2019 Feb 5.53	+296.4	Keck	LRIS	2000	3200–10,000
2019 May 3.17	+382.5	Magellan-Clay	LDSS-3	860	4250–10,000

Note. Phase is the observer frame days since the *B*-band maximum light (MJD 58221.41).

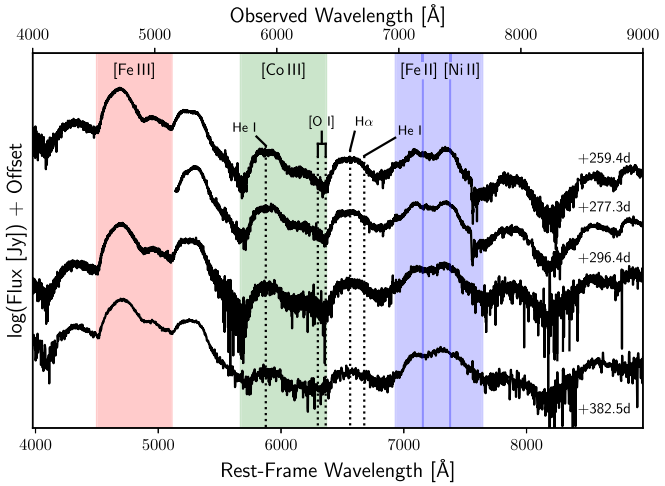

Figure 2. The dereddened spectra of SN 2018aoz obtained from four epochs during the nebular phase as labeled on the right side of the figure in days since the *B*-band maximum are shown. The spectra are vertically offset for display clarity. The vertical shaded colored regions show the locations of the broad emission features of [Fe III] (red), [Co III] (green), as well as [Fe II] and [Ni II] (blue) that are visible. While the [Fe III] and [Co III] features are produced by a blend of several broad emission lines, the [Fe II] and [Ni II] features are thought to be primarily due to transitions of [Fe II] λ7155 Å and [Ni II] λ7378 Å (vertical solid lines), respectively (Maeda et al. 2010b). The dotted vertical lines show the expected locations of narrow emission lines associated with nondegenerate companions and CSM in Type Ia SNe: Hα, He I, and [O I]. None of these narrow emission lines are detected. These spectra are available to the public in WISeREP https://www.wiserep.org.

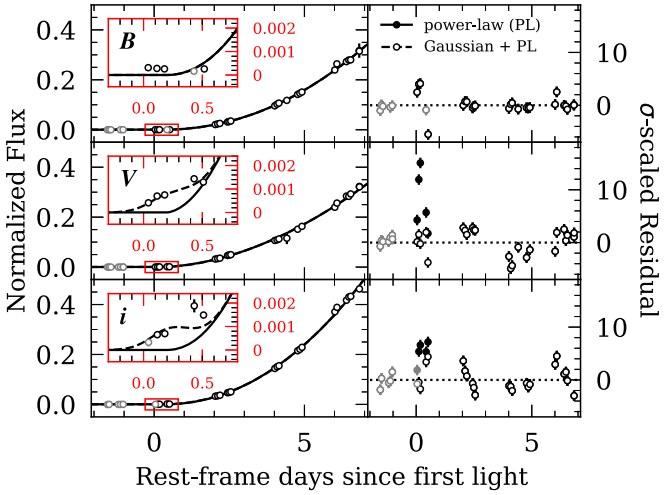

Figure 3. (Left) The dereddened early *BVi*-band (top to bottom) forced photometry light curves (circles) of SN 2018aoz up to 40% of the maximum light in the rest frame are compared to the best-fit power law + Gaussian (dashed curves) and its power-law component alone (solid curves). The data points with S/N < 3 are grayed out. The inset zooms in on the infant phase ($\lesssim$1 day). (Right) The σ-scaled residual of each data point for the best-fit power law + Gaussian (open circles) and its power-law component alone (closed circles) are shown over the same time interval as that in the left panel.

2.3. Host Galaxy, Distance, and Reddening

SN 2018aoz is located at (R.A., decl.) = ($11^{\rm h}51^{\rm m}01\overset{\rm s}{.}80$, $-28°44'38\overset{''}{.}5$) (J2000), in the halo of its host galaxy NGC 3923 (Paper I). We adopt the host galaxy redshift of $z = 0.0058$, distance modulus of 31.75 ± 0.08 mag based on normal Type Ia SN template fitting, and extinction correction of $E(B-V) \sim 0.09$ mag, consistent with the observed Na I D lines in the spectrum of SN 2018aoz as well as the expected Galactic extinction toward the source (Paper I). The extinction toward the source is also confirmed by fitting the observed color evolution of SN 2018aoz during the Lira law phase as detailed in Appendix A.

3. Early Evolution and Classification

3.1. Early Light Curves and the Characteristics of the Infant-phase Excess Emission

The infant-phase light curves of SN 2018aoz contain the lowest luminosity detected signals from an early Type Ia SN to date, reaching a depth of -10.5 absolute *AB* magnitude. In Paper I, we reported that the dominant source of its early luminosity appears to follow a power-law evolution. The observed *BVi*-band light curves over 1–7 days since the first light (or up to $\sim$40% of peak brightness) follows $L_\nu \sim t^{\alpha_\nu}$, consistent with the majority of other Type Ia SNe that have been observed in these phases (Nugent et al. 2011; Foley et al. 2012; Olling et al. 2015; Cartier et al. 2017; Holmbo et al. 2019; Miller et al. 2020b; Moon et al. 2021; Ni et al. 2022). The measured power-law indices for SN 2018aoz, $\alpha_{(B,V,i)} = (2.24, 1.99, 2.26)$, are also close to the Type Ia population average ($\alpha = 2.01$; Miller et al. 2020b). In principle, a power-law rise is expected for SNe powered by a smooth, centrally concentrated ^{56}Ni distribution with a power-law-like tail toward the ejecta surface, where α depends on the steepness of the tail (Piro & Nakar 2014). However, in addition to this component, we also found evidence for excess emission over the power law in the *V* and *i* bands during the first 0–1 day since the first light. This infant-phase excess emission is present during the same epochs as the *B*-band plateau, which has been attributed to line-blanket absorption by an over-density of Fe-peak elements near the ejecta surface. While in Paper I, we highlighted that excess radioactive heating by those same Fe-peak elements is one possible explanation for the excess emission, a range of other possible explanations and their implications remains to be thoroughly explored.

Here, we characterize the properties and statistical significance of the infant-phase excess emission in SN 2018aoz. Figure 3 (left panels) shows the results of fitting the early light curves of SN 2018aoz during 0–7 days with a power-law + excess emission, where the infant-phase excess emission is

modeled by a Gaussian in each of the V and i bands. (Note that the B-band light curve during 0–1 day is excluded from the fit since it is affected by B-band suppression.) The V- and i-band infant-phase light curves share the same Gaussian central epoch, μ, and width, σ, but each Gaussian is scaled independently. In each of the BVi bands, the power-law component has the form $L_\nu \propto (t-t_{\rm PL})^{\alpha_\nu}$, where the onset of the power law $t_{\rm PL}$ is shared among the bands while the power-law indices α_ν and scalings are independent parameters in each band. The best-fit power-law + excess emission (dotted curves in Figure 3) is obtained with $\mu = 0.25$ day since the first light and $\sigma = 0.17$ day for the Gaussian component, and $t_{\rm PL} = 0.19$ day since the first light and $\alpha_{(B,V,i)} = (2.1, 1.8, 2.1)$ for the power-law component (represented by the solid curves), which appears to adequately fit the observed early light curves (minus the excluded B-band light curve during 0–1 day). The reduced χ-squared statistic ($=\chi^2$ normalized by the number of degrees of freedom; $\chi^2_{\rm R}$) of 4.0 for this fit is significantly better than the one obtained by fitting a pure power law to the same light curves ($\chi^2_{\rm R} = 9.2$; Paper I), indicating that the Vi-band excess emission component is required to explain the observed light curves.

The statistical significance of the Vi-band excess emission is displayed in Figure 3 (right panels), showing the σ-scaled residual of the best-fit power-law + excess emission (open circles) compared to that of the power-law component alone (closed circles). The residuals of the power-law component appear to be dominated by the data points from the infant phase. Note that this is consistent with the $\chi^2_{\rm R}$ analysis of the power-law fitting in Paper I, where the $\chi^2_{\rm R}$ error from fitting a pure power law ($\chi^2_{\rm R} = 9.2$) was found to be predominantly from the infant-phase data points (with $\Delta\chi^2_{\rm R} = 6.0$) than from all subsequent data points (with $\Delta\chi^2_{\rm R} = 3.2$). Meanwhile, the power-law + excess emission model significantly reduces the residuals of the Vi-band data points from the infant phase, which now provides residuals similar to the data points from later phases. Thus, the early light curves of SN 2018aoz appear to require the distinct excess emission component peaked between ∼0.08 and 0.42 day since the first light. During this phase, excess emission is the dominant component of the SN light curve, emitting a total of $\sim 2.4 \times 10^{-9}$ erg cm^{-2} into the V and i bands along the line of sight (or $\sim 1.4 \times 10^{44}$ erg, assuming spherically symmetric emission). In Section 5, we examine potential mechanisms that can produce the observed excess emission.

3.2. Color Evolution

Figure 4 presents high-cadence KMTNet color curves of SN 2018aoz in $B - V$ (top) and $V - i$ (middle) aligned with its i-band light curve (bottom). The observations, which are nearly simultaneous among different filters, were linearly interpolated to the union of the two sets of epochs for each pair of adjacent filters during subtraction. The four vertical dotted lines in the figure mark four epochs, −14.4, −4.6, 10.4, and 26.0 days since the B-band maximum, where the colors undergo notable phase transitions in their evolution.

The $B - V$ color evolution of SN 2018aoz prior to the first color transition epoch, corresponding to the infant phase, was discussed extensively in Paper I. The simultaneous plateau in the B band and rapid rise in the V- and i-band light curves at these early times lead to an abrupt redward evolution wherein

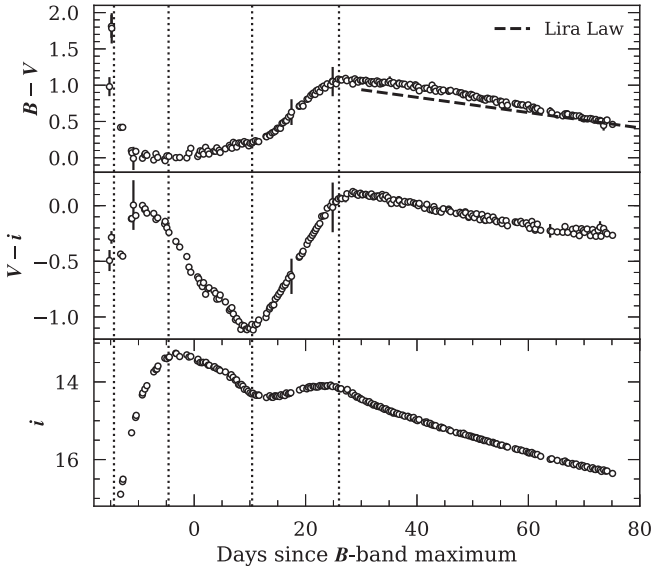

Figure 4. The observed (non-dereddened) optical colors of SN 2018aoz (black circles) in $B - V$ (top) and $V - i$ (middle) aligned with its i-band light curve (bottom). The data are binned over 0.3 day intervals. The vertical dotted lines mark the epochs of −14.4, −4.6, 10.4, and 26.0 days since the peak where the optical colors undergo notable phase transitions in their evolution (Moon et al. 2021). The dashed line denotes the Lira law from Burns et al. (2014). Note that a zoomed-in plot of the un-binned early color evolution focused on the early phases before ∼−8 days is shown in Figure 10.

the $B - V$ color changes by 1.5 mag between 1.0 and 12.4 hr after the first light. We refer to this redward color evolution as the *natal red bump* (NRB), hereafter, while the *NRB phase* refers to the epochs (∼1.0–12.4 hr) where the NRB is observed. The NRB is also identifiable in the $V - i$ color, though with a smaller color change of 0.23 mag between 2.8 and 12.2 hr. During the NRB phase, the average $B - V$ color is ∼1.7 mag redder than the average $V - i$ color, consistent with the presence of Fe absorption lines that selectively suppress the B band.

The entire color evolution after the first color transition epoch is largely consistent with those of other normal Type Ia SNe, and is best described in relation to the i-band light curve (Moon et al. 2016) as detailed in Appendix A.

Figure 5 presents the Swift UV-optical color curves of SN 2018aoz compared to those of other Type Ia SNe. The near-peak UV-optical colors of normal Type Ia SNe have been grouped into two categories (Milne et al. 2013): near-UV (NUV) red (e.g., SN 2017cbv; Hosseinzadeh et al. 2017) and NUV blue (e.g., SN 2011fe; Brown et al. 2012). Brown & Sand (2018) initially reported that SN 2018aoz displayed blue UV-optical colors that are similar to Type Ia SNe with super-Chandrasekhar ejecta masses (Brown et al. 2014). Indeed, prior to the peak, the colors are bluer than SN 2011fe, which is one of the bluest events in the NUV-blue group (Brown et al. 2017). However, subsequent evolution shows that while lying on the blue edge of the group, SN 2018aoz overall appears to follow the NUV-blue group. In particular, the observed colors near the peak are not as extreme as those of the super-Chandrasekhar-mass events—for instance, SNe 2012dn and 2011aa (Figure 5; Brown et al. 2014).

3.3. Classification

We classify SN 2018aoz as a normal Type Ia SN that is intermediate between the CN/NV and BL/HV subtypes based

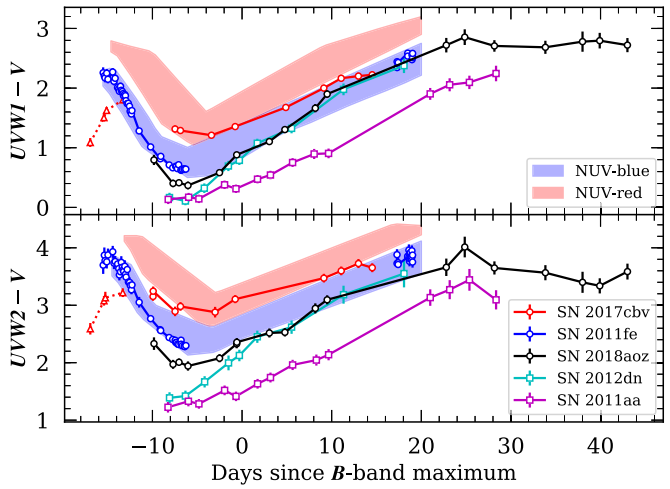

Figure 5. The observed (non-dereddened) UV-optical colors of SN 2018aoz (black open circles) in $UVW1 - V$ (top) and $UVW2 - V$ (bottom) compared to those of SN 2017cbv (red circles; Hosseinzadeh et al. 2017), SN 2011fe (blue circles; Brown et al. 2012), the NUV-red/blue groups of normal Type Ia SNe (colored shaded areas, Milne et al. 2013), and the super-Chandrasekhar-mass Type Ia SNe 2012dn and 2011aa (cyan and magenta squares, respectively; Brown et al. 2014). The red triangles represent the color of SN 2017cbv during its early excess emission.

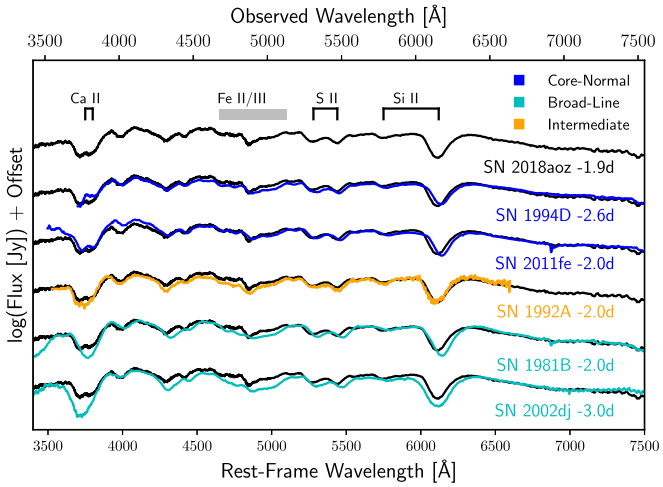

Figure 6. The dereddened spectrum of SN 2018aoz (black solid line; Paper I) taken 1.9 days before the B-band maximum is compared to spectra of Type Ia SNe of different subtypes obtained at comparable epochs: SN 1994D (Meikle et al. 1996) and 2011fe (Parrent et al. 2012) (core-normal subtype; blue); SN 1981B (Branch et al. 1983) and SN 2002dj (Pignata et al. 2008) (Broad-Line subtype; cyan); SN 1992A (Kirshner et al. 1993) (intermediate type; orange). Observed absorption features of Ca II, Fe II/III, S II, and Si II are labeled at the top of the panel.

on its spectral properties as follows. (Note that the SN light curves also support this classification as detailed in Appendix B.) Figure 6 compares the spectrum of SN 2018aoz taken 1.9 days before the B-band maximum (Paper I) to spectra of normal Type Ia SNe from the CN and BL subtypes of Branch et al. (2006): SNe 1994D (CN subtype; Meikle et al. 1996), 2011fe (CN subtype; Parrent et al. 2012), 1981B (BL subtype; Branch et al. 1983), 2002dj (BL subtype; Pignata et al. 2008), and 1992A (intermediate between CN and BL; Kirshner et al. 1993) from a similar phase. The spectrum of SN 2018aoz is consistent with those of the other normal Type Ia SNe overall, whereas the detailed shapes of key absorption features seem to be intermediate between CN and BL events. The sharp Fe II/III absorption features seen in the spectrum of SN 2018aoz are typical of CN events (e.g., SNe 1994D and 2011fe; blue spectra); however, the Ca II and Si II absorption features of SN 2018aoz are relatively strong, which is a step in the direction of typical BL events such as SNe 1981B and 2002dj (cyan spectra). SN 1992A (orange spectrum), classified as marginally BL while bordering CN (Branch et al. 2006), is the closest spectroscopic analog to SN 2018aoz with nearly identical features in the figure, suggesting that SN 2018aoz is also intermediate between CN and BL.

Figure 7 compares the evolution of the velocity of the Si II λ6355 Å feature (Si II velocity, hereafter) of SN 2018aoz (Paper I) to what is expected for the NV and HV subtypes of Type Ia SNe. Note that the NV events (e.g., SN 2011fe; blue triangles) are characterized by near-peak Si II velocities of about $(10.6 \pm 0.4) \times 10^3$ km s^{-1}, while the HV events (e.g., SN 2002dj; cyan triangles) have higher near-peak Si II velocities in the range of $\sim$(11.8–17.0) $\times 10^3$ km s^{-1} (vertical cyan interval; Wang et al. 2009). The NV and HV subtypes largely overlap with CN and BL, respectively (Parrent et al. 2014). The Si II velocity evolution of SN 2018aoz (orange circles) during early (<-5 days since the B-band maximum) and late (>15 days) evolutionary phases appears to follow the NV subtype (blue curve with shaded area). Around the peak

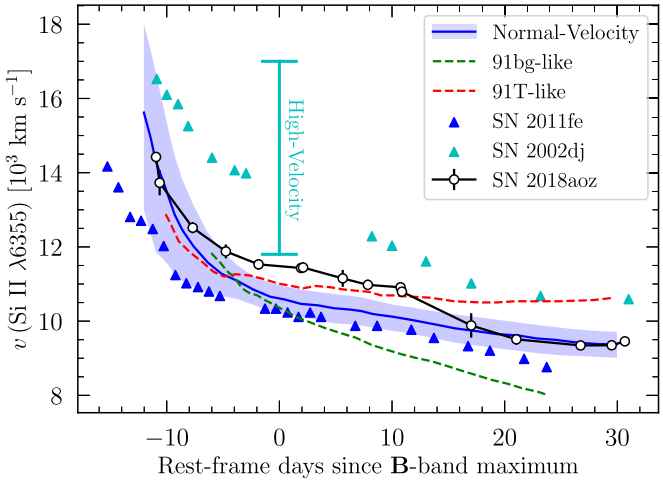

Figure 7. The observed velocity evolution of the Si II spectral feature of SN 2018aoz (orange circles; Paper I) is compared to the average velocity evolution for NV Type Ia SNe (blue solid curve with shaded 1σ error region; Wang et al. 2009) as well as that of 91bg-like (green-dashed curve) and 91T-like (red-dashed curve) events in the rest frame. SNe 2011fe (blue triangles; Pereira et al. 2013) and 2002dj (cyan triangles; Pignata et al. 2008) are examples of NV and HV events, respectively, with $\Delta M_{15}(B)$ similar to that of SN 2018aoz.

between ~ -5 and 15 days, however, its velocity becomes significantly higher than that of the NV population and approaches those of HV events. The peak Si II velocity of $(11.4 \pm 0.1) \times 10^3$ km s^{-1} in SN 2018aoz is about 2σ higher than the NV population average and near the lower boundary of the HV subtype. Following the peak, the average Si II velocity gradient of SN 2018aoz is -68 km s^{-1} day^{-1}, which is on the boundary between the high-velocity gradient and low-velocity gradient subclasses of Type Ia SNe (Benetti et al. 2005) that roughly correspond to HV and NV, respectively (Parrent et al. 2014). The expected Si II velocity evolutions of 91bg-like (green-dashed curve) and 91T-like (red-dashed curve), the two most common peculiar types of Type Ia SNe, are apparently

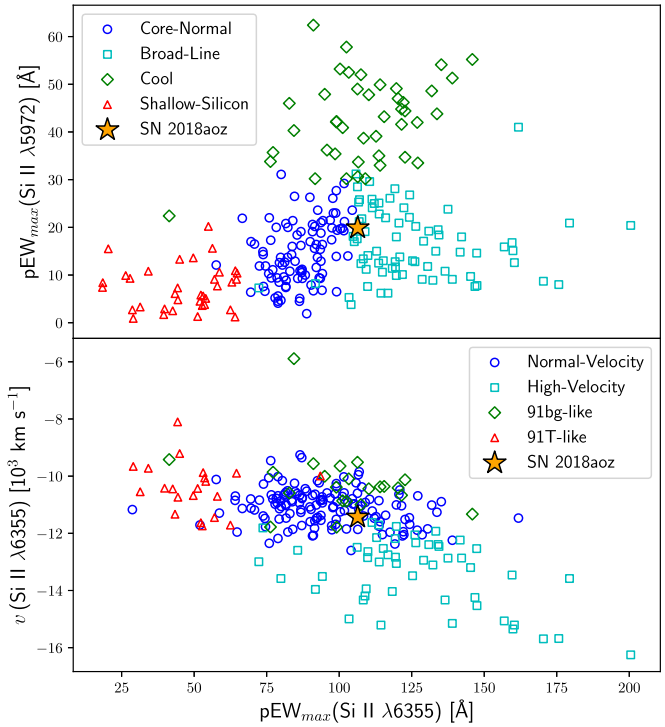

Figure 8. Comparison of pEW widths of Si II lines (top) and Si II velocity (bottom) of SN 2018aoz (orange star) with those of other Type Ia SNe (Blondin et al. 2012). The colored symbols represent events from the four main subtypes of Type Ia SNe: CN/NV (blue circles), BL/HV (cyan squares), cool/91bg-like (green diamonds), and shallow-silicon/91T-like (red triangles). Note that BL/NV and CN/BL are both subsets of normal Type Ia SNe, while cool/91bg-like and shallow-silicon/91T-like are considered peculiar.

different from that of SN 2018aoz shown in Figure 7 during late ($\gtrsim$15 days since the *B*-band maximum) evolutionary phases. Thus, the Si II velocity evolution of SN 2018aoz also supports its intermediate nature between NV/CN and HV/BL, while it is clearly incompatible with those of the prototypical peculiar subtypes.

The intermediate nature of SN 2018aoz between the normal subtypes of CN and BL is confirmed by the pseudo-equivalent widths (pEWs) of Si II lines from its spectrum taken 1.9 days prior to the *B*-band maximum. We measure pEWs of 20.22 and 106.4 for the Si II 5972 Å and 6355 Å lines, respectively, using the method of Branch et al. (2006). Figure 8 compares the peak Si II pEWs and Si II velocity of SN 2018aoz to those of a sample of Type Ia SNe (Blondin et al. 2012) from the CN/NV (blue circles) and BL/HV (cyan squares) subtypes, as well as the peculiar 91bg-like (or *shallow-silicon*; red triangles) and 91T-like (or *cool*; green diamonds) subtypes. The parameters of SN 2018aoz are located at the boundary between the CN/NV and BL/HV subtypes of normal Type Ia SNe in both panels. The Si II pEWs of SN 2018aoz (top panel) are consistent with BL events with Si II 6355 Å pEW $>$105 (Blondin et al. 2012), while the Si II velocity of SN 2018aoz (bottom panel) is consistent with NV events with Si II velocity $<11.8\times10^3$ km s^{-1}, leading to the intermediate classification between the BL/(HV) and NV/(CN) subtypes.

4. Early Light-curve Constraints on the Companion

Early observations of Type Ia SNe have been used to search for excess emission due to ejecta collision with companions (e.g., Bloom et al. 2012; Olling et al. 2015; Marion et al. 2016; Hosseinzadeh et al. 2017, 2022; Dimitriadis et al. 2019; Li et al. 2019; Shappee et al. 2019; Moon et al. 2021). With early light curves from the low brightness of -10.5 absolute *AB* magnitudes, observations of SN 2018aoz probe the luminosities expected not only for nondegenerate, but also WD companions for the first time. It, therefore, provides a unique opportunity to search for such emission and places strict constraints on the nature of the companion star. Here, we compare the light curves of SN 2018aoz with the analytic ejecta-companion interaction model of (Kasen 2010, K10 hereafter) that has been widely adopted for this type of analysis. The luminosity (Γ) and effective temperature of the interaction emission in the model depend on the size of the companion (related to the binary separation distance in Roche overflow), as well as the opacity, mass, and kinetic energy of the ejecta. When observed with a viewing angle θ, the luminosity is $\Gamma\times S(\theta)$, where

$$S(\theta)\simeq 0.982\times\exp[-(\theta/99.7)^2]+0.018 \quad (1)$$

describes the angle dependence of the observed luminosity (Olling et al. 2015). Note that the emission is strongest when the progenitor system is observed from the side of the companion star (0°; $S=1$) and it is weakest from the side of the progenitor star (180°; $S=0.056$).

4.1. Comparison to Fiducial Models

Figure 9 (left panels) compares the early *Vri*-band light curves of SN 2018aoz (black-filled circles) during 0–3 days since the first light with what is predicted by the K10 model for three cases of nondegenerate binary companions at $\theta=0°$ in Roche overflow: 1 $M_\odot$ red giant (1RG; red solid curve), 6 $M_\odot$ main-sequence subgiant (6MS; blue solid curve), and 2 $M_\odot$ main-sequence subgiant (2MS; indigo solid curve). In the K10 model, we adopt the electron scattering opacity of $\kappa=0.2$ cm^2 g^{-1} for H-poor Type Ia SN ejecta and the ejecta mass and kinetic energy of 0.80 $M_\odot$ and 0.63 $\times10^{51}$ erg, respectively, for SN 2018aoz (Paper I). For all three cases, the predicted emission is brighter than the observed luminosity, disallowing those configurations for the progenitor system under the K10 model. The *B*-band light curve during 0–1 day was excluded from our comparisons because it is affected by *B*-band suppression while the K10 model assumes a pure blackbody spectral energy distribution. Note that the values of ejecta mass and kinetic energy we adopted are the lower limits of the ranges,$\sim$0.8–1.0 $M_\odot$ and $\sim$(0.6–0.8) $\times10^{51}$ erg, respectively, that have been considered for SN 2018aoz (Paper I). Since larger ejecta mass and kinetic energy both lead to brighter emission in the K10 model, the constraints provided in Figure 9 against the companion are conservative with respect to ejecta mass and kinetic energy. (While *B*-band light curves have usually been used in the search for ejecta-companion interaction emission, we show in Appendix C that model comparisons with the suppressed *B*-band light curve in the infant phase over-constrains the companion in the case of SN 2018aoz.)

The K10 model is based on the assumption of local thermodynamic equilibrium (LTE) between the shock-heated ejecta and its radiated emission. According to Kutsuna & Shigeyama (2015, KS15 hereafter), the matter-radiation coupling may not be strong enough to reach LTE due to the low gas density in the ejecta-companion interaction, indicating that the K10 model may overestimate the emission temperature

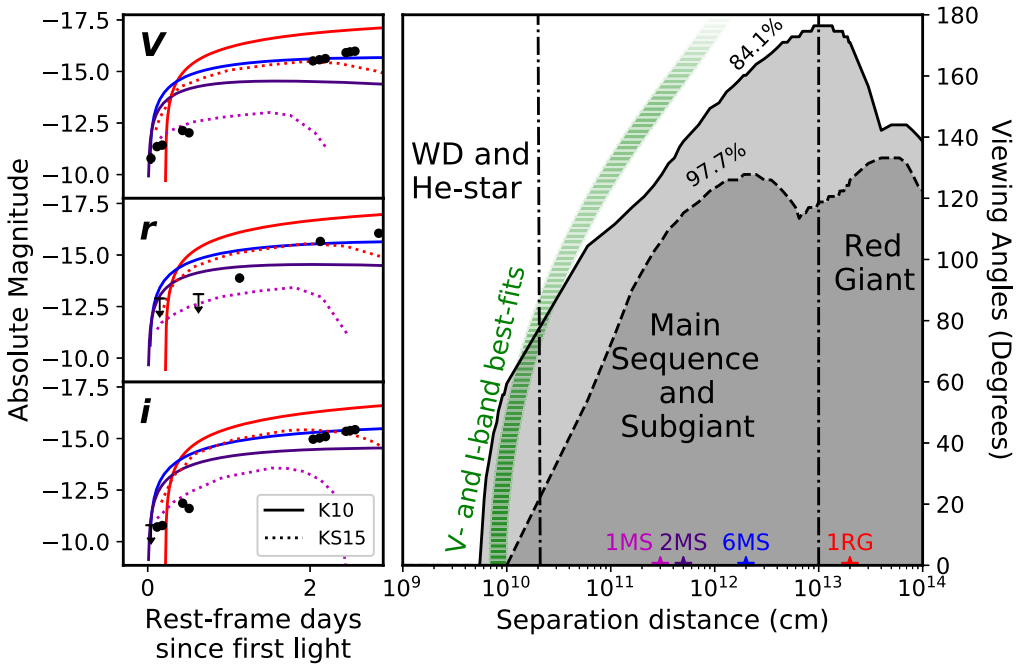

Figure 9. (Left) The dereddened early *Vri*-band (from top to bottom) light curves of SN 2018aoz (black circles) within 3 days after the first light in the rest frame are compared to ejecta-companion interaction models with 0° viewing angle. The models are of the 2MS (indigo solid curves), 6MS (blue solid curves), and 1RG (red solid curves) companions from Kasen (2010) as well as the 1MS (magenta dotted curves) and 1RG (red-dotted curves) companions from Kutsuna & Shigeyama (2015). The black inverted arrows are 3σ detection limits. (Right) The parameter space of separation distances and viewing angles of possible progenitor systems is shown. The vertical dotted–dashed lines divide the *x*-axis (binary separation distance) into WD and He star, main-sequence and subgiant, and RG regimes. The parameters in the shaded area underneath the solid and dashed black curves are ruled out at 84.1% and 97.7% confidence levels, respectively, by the early light curves of SN 2018aoz and the model predictions of Kasen (2010). The magenta, indigo, blue, and red stars at the bottom of the panel show the parameters for the correspondingly colored models in the left panels. The green-shaded region shows the best-fit separation distances obtained by fitting power-law + Kasen (2010) ejecta-companion interaction models for a set of viewing angles between 0° and 180° (see Section 5.2). The transparency of the green-shaded region is related to the goodness of the fit (χ^2_R), where darker shading corresponds to a better fit.

(and luminosity). Figure 9 (left panels) also compares the observed light curves with the predictions of the two cases of companions from KS15: 1RG (red-dotted curve) and 1MS ($1\,M_\odot$ main-sequence subgiant companion; magenta dotted curve), both at $\theta = 0°$ and in Roche overflow. While the 1RG case clearly overpredicts the observed emission at $\theta = 0°$, the case of 1MS is at a very similar brightness to what is observed during 0–0.5 day. We note, however, that KS15 excludes free–free emission and Compton scattering—two processes known to accelerate equilibrium (Weaver 1976; Katz et al. 2010)—in their estimation of the strength of matter-radiation coupling, likely leading to underprediction of emission temperature and luminosity. Furthermore, no underlying radioactive SN emission is included in the luminosity calculations by KS15 (and also by K10). Therefore, it is highly likely that the $\theta = 0°$ 1MS case is also disallowed given the close similarity between its prediction and the observed brightness, though it is difficult to precisely quantify the effects of excluding the two radiation processes and the underlying SN emission in the predicted luminosities. For the predicted luminosities of ejecta-companion interaction alone, the KS15 and K10 models may be regarded as providing upper and lower bounds, respectively.

4.2. Companion Constraints from Generalized Modeling

We generalize our analysis using the K10 model to allow for ejecta-companion interactions from all possible viewing angles between 0° and 180° and binary separation distances in the range of 10^9–10^{14} cm, following the methods of Moon et al. (2021). The range of separation distances corresponds to those of companions as small as WDs and as large as red supergiants at the Roche limit. The right panel in Figure 9 shows the extent of this parameter space, where the separation distances are divided into the regimes of WD and He star, main sequence and subgiant (MS), and red giant (RG) with two vertical dotted–dashed lines approximating the lower bounds for the MS (von Boetticher et al. 2017) and late-phase RG cases (Seeds 1984). By comparing the models represented by pairs of these parameters (i.e., viewing angle and separation distance) with the observed luminosities and pre-detection upper limits, we obtain the solid and dashed curves in the figure, representing the lower limits of acceptable viewing angles as a function of separation distance (i.e., the area under the curve is ruled out) for the 84.1% and 97.7% confidence levels, respectively.[42] The confidence levels account for photometry errors as well as those of the model parameters, including redshift, explosion epoch, ejecta mass, and ejecta kinetic energy, estimated using a bootstrap method, assuming Gaussian error distribution. Note that there are additional systematic uncertainties in the model comparison as mentioned in Section 4.1 above: those associated with (1) the adoption of lower limits for the ejecta mass and kinetic energy of SN 2018aoz and (2) the exclusion of the radioactive SN emission, which are not included in our analysis. However, both of these uncertainties only allow for stronger constraints against the companion (see Section 4.1). The assumption of Roche overflow may also break if there is a long spin-down

[42] Note that 84.1% and 97.7% correspond to the 1 and 2σ levels, respectively, of a Gaussian distribution in one direction.

phase before the SN explosion during which the binary separation distance can evolve (Meng & Li 2019).

Based on the comparison shown in Figure 9 (right panel), a low-mass ($\lesssim$ a few solar mass) main-sequence star or subgiant at a high ($\gtrsim$80°) viewing angle, He star, or WD are the most likely binary companions in SN 2018aoz. Note that these results are independent of whether ejecta-companion interaction emission has really been detected in SN 2018aoz. Separation distances from $\sim 5 \times 10^{11}$ to $\sim 10^{14}$ cm, corresponding to companions larger than 2MS, are disallowed (at an 84.1% confidence level) for most ($\gtrsim$80% of) of the viewing angles because the expected luminosity from their ejecta-companion interaction emission would exceed the observed luminosity of SN 2018aoz in the first 3 days for $\theta < 140°$–$175°$. Thus, under the K10 model, if SN 2018aoz had a large main-sequence or RG companion, it would need to have been located within a small range of viewing angles behind the SN. The ejecta-companion interaction luminosity can be significantly lower than the K10 model predicts if LTE is not reached, as mentioned above, with KS15 providing a lower bound. However, if we adopt the KS15 model for the 1RG case, the luminosity of 1RG (red-dotted curve in Figure 9, left panels) would be similar to that of 6MS in the K10 model (blue solid curve), for which ~90% of viewing angles are still ruled out (Figure 9, right panel). Therefore, the presence of an RG companion is very unlikely even if the LTE assumption of K10 is not satisfied. Although there is a small region in the upper-right corner (i.e., large separation and viewing angle) of Figure 9 that is not directly ruled out by the comparison, the separation distances correspond to short-lived companions (e.g., red supergiants), which are very unlikely to be found in the halo region of an elliptical galaxy—where SN 2018aoz is located—due to the lack of recent star formation (see Section 8.1).

5. Infant-phase Excess Emission Modeling

SN 2018aoz shows significant excess emission over the power-law rise during 0–1 day since the first light (Section 3.1). An over-density of ^{56}Ni near the ejecta surface can produce excess thermal emission in this phase (Paper I), but other possibilities—such as ejecta shock interaction—and their subsequent implications for the progenitor system remain unexplored. We examine the origin of the infant-phase excess emission by fitting the early light curves of SN 2018aoz using a model combining the underlying SN emission (which is represented by a power law; see Section 3.1) and excess emission. We compare the fits obtained using models of four conceivable mechanisms for the excess emission: surface ^{56}Ni heating (Section 5.1), ejecta-companion interaction (Section 5.2), ejecta-CSM interaction (Section 5.3), and shock breakout (Section 5.4). Note that the characteristic ejecta velocity of SN 2018aoz, estimated using its observed peak Si II velocity of 11,400 km s^{-1} (Paper I), broadly constrains the possible sources of infant-phase emission from ejecta shock interactions to be within $\lesssim 10^{14}$ cm of the progenitor, which includes only the binary companion, nearby CSM, and the shock-heated progenitor surface.

For all of the four excess emission mechanisms, we adopt blackbody spectral energy distributions because they are based on thermal processes. We fit the light curves of SN 2018aoz during 0–8 days, but exclude the *B*-band light curve during 0–1 day since it is affected by *B*-band suppression and incompatible with a pure blackbody process (Paper I). The results obtained using the four models are compared below, followed by detailed descriptions of each model and the fitting process in the subsequent subsections.

Figure 10 compares the dereddened colors, $(B-V)_0$ (top-left panel) and $(V-i)_0$ (bottom-left panel), and *BVi* light curves (right panels) of SN 2018aoz with the best-fit model predictions: blue-dashed curves for surface ^{56}Ni heating, green-dashed curves for ejecta-companion interaction, and red-dashed curves for ejecta-CSM interaction. (Shock breakout is not shown because it is too faint to be compared for a reasonable set of model input parameters; Section 5.4.) The fit quality is not significantly different for the three best fits, which have similar χ^2_R values of 3.4, 3.5, and 3.2, respectively. As can be seen in the figure, all three models appear to reproduce the observed *Vi*-band light curves of SN 2018aoz as well as the $V-i$ color curve similarly well; however, these blackbody excess emission models all over-predict the *B*-band luminosity by ~0.5−1.0 mag in 0.1–0.5 day, leading to bluer $B-V$ color than observed during the period. Note that the lower infant-phase *B*-band luminosity compared to the *V* and *i* bands in SN 2018aoz, which is incompatible with pure blackbody emission, has been attributed to *B*-band suppression caused by surface Fe-peak elements (Paper I). As detailed in the following subsections, the best-fit parameters of the surface ^{56}Ni heating, ejecta-companion interaction, and ejecta-CSM interaction models are all compatible with viable physical processes that can produce the observed infant-phase excess emission in SN 2018aoz.

5.1. Radioactive Heating by Excess Surface ^{56}Ni

We first fit the observed early light curves of SN 2018aoz using the combination of power-law emission (for the underlying SN emission) and the emission from a ^{56}Ni shell distribution (for surface ^{56}Ni heating). For the power-law component, we use the power law described in Section 3.1 with onset t_{PL} and indices $\alpha_{(B,V,i)}$. For the infant-phase ^{56}Ni shell emission, we developed the following model in three steps:

1. We adopt the luminosity calculation for ^{56}Ni-powered SNe from (Piro & Nakar 2014, PN14 hereafter) based on ^{56}Ni decay and photon diffusion. In the model, the SN luminosity is determined by the ^{56}Ni distribution and the *diffusion depth*, defined as the deepest layer in the ejecta that is visible via photon diffusion. For the evolution of the diffusion depth, we adopt the following equation from Paper I (based on Equation (1) in PN14) describing the fractional mass of the ejecta ($\Delta M/M_{ej}$) in the layers above the diffusion depth at $t-t_0$ days since explosion:

$$\frac{\Delta M}{M_{ej}} \approx 1.3\left(\frac{t-t_0}{\tau_m}\right)^{1.76} \quad (2)$$

$$\tau_m = \left(\frac{\kappa}{13.8\,c}\right)^{1/2}\left(\frac{6\,M_{ej}^3}{5\,E_{ej}}\right)^{1/4}, \quad (3)$$

where τ_m is the geometric mean of the diffusion and expansion timescales (Arnett 1982; Moon et al. 2021) related to the ejecta mass, ejecta kinetic energy, and opacity (M_{ej}, E_{ej}, and κ, respectively). We use the value of $\tau_m = 9.51 \pm 0.26$ measured from the bolometric light

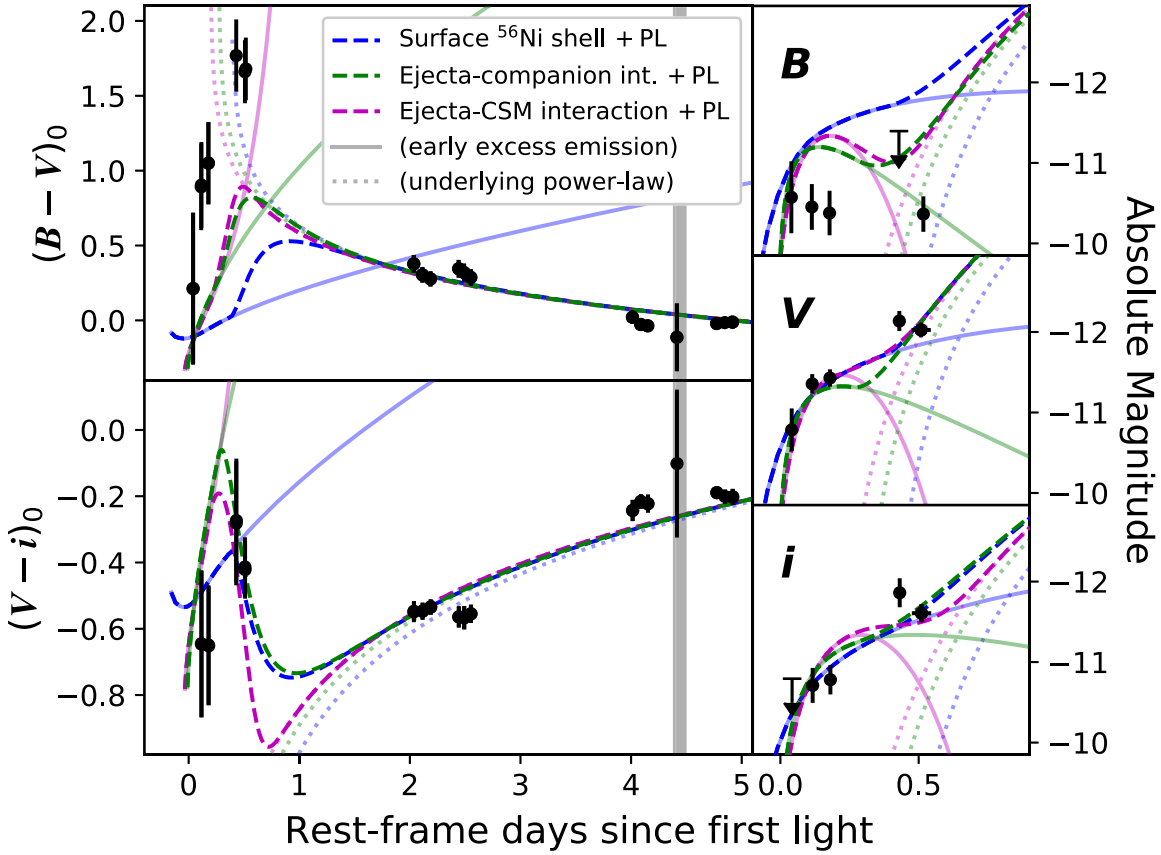

Figure 10. (Left) The dereddened $B-V$ (top) and $V-i$ (bottom) colors of SN 2018aoz in the rest frame (circles) are compared with what is expected from the power law (PL) + three models of early excess emission in Type Ia SNe: (1) surface ^{56}Ni heating (blue-dashed curves; Section 5.1), (2) ejecta-companion interaction (green-dashed curves; Section 5.2), and (3) ejecta-CSM interaction (magenta dashed curves; Section 5.3). The transparent solid and dotted curves show the early excess emission and underlying power-law components, respectively, of each correspondingly colored model. The vertical gray line marks the epoch when the first spectrum was taken (4.4 days since the first light or −11.0 days since the peak). (Right) The dereddened *BVi*-band (from top to bottom) light curves of SN 2018aoz in the rest frame are compared with those predicted by the same models from the left panels. The inverted arrows are detection limits at an S/N of 3.

curve of SN 2018aoz (Paper I). Note that the explosion epoch, t_0, can be different than the onset of the power-law component of the light curve, $t_{\rm PL}$, due to the possibility of a few hours to days delay (or *dark phase*; Piro & Nakar 2013, 2014) before the diffusion depth reaches the underlying main distribution of centrally concentrated ^{56}Ni in the ejecta, which is responsible for the power-law rise (Section 3.1).

2. The ^{56}Ni distribution in PN14 (described by a logistic function; see Equation (11) therein) is replaced by the ^{56}Ni shell distribution with the following functional form:

$$X_{56}(t) = \begin{cases} X_s, & t - t_0 < t_s \\ 0, & t - t_0 > t_s, \end{cases} \quad (4)$$

where $X_{56}(t)$ is the mass fraction of ^{56}Ni at the diffusion depth at t–t_0 days since explosion and t_s is the time when the diffusion depth reaches the inner radius of the shell. (Note that the time coordinate t is related to the radial mass coordinate of the diffusion depth by Equation (2).) In the fitting below, we represent the distribution using two physical parameters, t_s and M_s, where $M_s = X_s \Delta M(t_s)$ is equal to the total mass of ^{56}Ni above the diffusion depth at time t_s in the ejecta.

3. The ^{56}Ni shell emission, originating from radioactive heating of the high-density SN ejecta in infant phases, is assumed to be blackbody distributed (i.e., we assume that the emission is fully thermalized and that gamma rays are fully trapped) in order to fit the multi-band SN light curves. We estimate the blackbody temperature, or *color temperature* (T_c), of the ^{56}Ni shell emission using the following equation (based on Equation (12) from Piro & Nakar 2013):

$$T_c^4 = \frac{L\tau_s}{4\pi\sigma_{SB} r_{\rm ph}^2}, \quad \tau_s = \tau_c \left(\frac{r_{\rm ph}}{r_c}\right)^2, \quad (5)$$

where L is the luminosity of the ^{56}Ni shell emission; $r_{\rm ph}$ is the radius of the photosphere; and τ_s is a parameter combining the radius, r_c (or *color depth*), in the ejecta where the ^{56}Ni radioactive emission is thermalized and the optical depth, τ_c, at the color depth. We estimate $r_{\rm ph}$ based on a polytropic ($n = 3$) ejecta profile expected for an exploding WD undergoing homologous expansion (Piro & Nakar 2013), and assume τ_s is roughly constant over the ∼1 day infant phase. Note that τ_s is expected to be close to unity since both τ_c and $r_{\rm ph}/r_c$ are typically not much larger than unity (Piro & Nakar 2013), so the assumption can at most contribute to an error with near-unity order.

Fitting the *BVi*-band light curves of SN 2018aoz up to 8 days since the first light, excluding the *B*-band light curve during 0–1 day, we obtain the best-fit power-law + surface ^{56}Ni heating model with $\chi^2_{\rm R} = 3.4$. The parameters are $t_0 = -0.17$ day, $t_s = 0.13$ day, $t_{\rm PL} = 0.38$ day, all since the epoch

of the first light (MJD 58206.00) in the rest frame, $M_s = 8.3 \times 10^{-4}\,M_\odot$, $\tau_s = 18.2$, and $\alpha_{B,V,i} = (2.03, 1.74, 2.08)$. For the properties of the early excess emission in the fit, we allowed for t_s in the range of 0.01–1.0 day, X_s in 1%–99%, and τ_s in 2/3–100. The best fit (blue-dashed curves in Figure 10) appears to provide an excellent match to the observed infant-phase excess emission of SN 2018aoz in the *V* and *i* bands with an $8.3 \times 10^{-4}\,M_\odot$ shell of excess ^{56}Ni in the outer 0.30% of the SN-ejected mass. If this is the origin of the infant-phase excess emission, then the difference between the best-fit t_0 and t_{PL} parameters indicates the presence of a ∼0.55 day dark phase in SN 2018aoz, similar in length to the one reported in the normal Type Ia SN 2011fe (∼0.5 day; Piro & Nakar 2014). We also note that the best-fit indices $\alpha_{B,V,i}$ are slightly lower than those obtained in Section 3.1, though they are still consistent with the $\alpha \sim 2$ expectation for power-law rise that has been found in other normal Type Ia SNe.

The best-fit mass and location of surface ^{56}Ni obtained above, $8.3 \times 10^{-4}\,M_\odot$ of ^{56}Ni in the outer 0.30% of the SN-ejected mass, are larger and deeper in the ejecta, respectively, than $1.8 \times 10^{-4}\,M_\odot$ of ^{56}Ni in the outer 0.31% of the SN-ejected mass obtained in Paper I by fitting the infant-phase excess emission of SN 2018aoz with a purely ^{56}Ni-powered blackbody model (as opposed to the power-law + surface ^{56}Ni model). These numbers are broadly comparable with the location and quantity of Fe-peak elements required to explain the *B*-band suppression associated with the NRB, $\sim 10^{-3}\,M_\odot$ in the outer ∼1% of the SN ejecta (Paper I). However, radiative transfer simulations that account for both line formation and incomplete gamma-ray trapping are required to determine if any single distribution of Fe-peak elements can reproduce both the infant-phase excess emission and NRB features in SN 2018aoz simultaneously. We discuss this in the context of thin-shell He-shell DDet simulations in Section 7, below.

5.2. Ejecta Interaction with the Companion

We model the infant-phase emission of SN 2018aoz with a combination of radioactive SN emission and ejecta-companion interaction emission—the former with a power law (Section 3.1) and the latter with the K10 model (Section 4). For the K10 model, we use the electron scattering opacity of $\kappa = 0.2\,\mathrm{cm^2\,g^{-1}}$ for H-poor Type Ia SN ejecta following Section 4. Fitting the observed *BVi* light curves during 0–8 days, excluding the *B*-band light curve during 0–1 day, we obtain the green-shaded region in Figure 9 (right panel) showing the distribution of the best-fit companion separation distances (a) for viewing angles (θ) between 0° and 180°. The upper and lower boundaries of the region were obtained using two cases of relatively small and large ejecta masses and kinetic energies, respectively, derived by modeling the light curves of SN 2018aoz (Paper I) as follows: (1) $M_{ej} = 0.80\,M_\odot$ and $E_{ej} = 0.63 \times 10^{51}$ erg based on the Arnett (1982) model; and (2) $M_{ej} = 1.05\,M_\odot$ based on He-shell DDet simulations, corresponding to $E_{ej} = 0.82 \times 10^{51}$ erg for the characteristic ejecta velocity of 11,400 km s^{-1}.

Table 3 shows the range of fit parameters obtained using different M_{ej}, E_{ej}, and θ. In the fit, we allowed for a in the range of 10^9–10^{13} cm, which includes all reasonable Roche separation distances for Type Ia SN progenitors (see Figure 9). The best-fit model light and color curves with $\theta = 0°$, which are nearly identical for the two cases of M_{ej} and E_{ej} (green-dashed curves in Figure 10), provide a very similar goodness of fit to those of SN 2018aoz as the best-fit surface ^{56}Ni heating model (Section 5.1). The differences between the onsets of the K10 and power-law components in the models ($=t_0$ and t_{PL}, respectively) range from ∼0.3 day for the lowest-χ^2_R case of $\theta = 0°$ to ∼0.6 day for the case of $\theta = 180°$. These differences are consistent with t_{PL}–t_0 of 0.54 day obtained with the surface ^{56}Ni heating model, pointing to an approximately half-day post-explosion delay (or dark phase) in SN 2018aoz for the diffusion of the radioactive SN emission responsible for the power-law rise. As can be seen in the table, the change in χ^2_R between $\theta = 0°$ and 180° is less than 2%, indicating that the goodness of fit of the ejecta-companion interaction model does not change significantly with separation distance (a) ranging from $(0.7–1.0) \times 10^{10}$ cm for $\theta = 0°$ to $(0.9–1.5) \times 10^{12}$ cm for $\theta = 180°$. These separation distances correspond to two types of companions that appear to be nearly equally compatible with the observed infant-phase excess emission of SN 2018aoz under the K10 model: (1) a low-mass ($\lesssim$ a few solar mass) main-sequence star or subgiant at $\gtrsim 80°$ viewing angle; or (2) a WD or He star at $\lesssim 80°$ viewing angle. Note that the case of ejecta interaction with a WD companion for the origin of the infant-phase excess emission implies a D∧6 origin for SN 2018aoz since it is the only scenario that predicts the presence of a surviving WD companion after the SN explosion.

Table 3
Ejecta-companion Interaction Model Fit Parameters

M_{ej} and E_{ej}	Viewing Angle	Fit Parameters	χ^2_R
$0.80\,M_\odot$ and 0.63×10^{51} erg[a]	$\theta = 0°$	$a = 1.0 \times 10^{10}$ cm $t_0 = -0.01$ day $t_{PL} = 0.27$ day $\alpha_{B,V,i} = (2.07, 1.77, 2.10)$	3.48 (lowest)
	$\theta = 180°$	$a = 1.5 \times 10^{12}$ cm $t_0 = -0.23$ day $t_{PL} = 0.37$ day $\alpha_{B,V,i} = (2.05, 1.75, 2.08)$	3.54
$1.05\,M_\odot$ and 0.82×10^{51} erg[b]	$\theta = 0°$	$a = 6.8 \times 10^9$ cm $t_0 = 0.00$ days $t_{PL} = 0.25$ day $\alpha_{B,V,i} = (2.08, 1.78, 2.11)$	3.47 (lowest)
	$\theta = 180°$	$a = 8.8 \times 10^{11}$ cm $t_0 = -0.19$ day $t_{PL} = 0.37$ day $\alpha_{B,V,i} = (2.04, 1.74, 2.08)$	3.52

Notes. t_0 and t_{PL} are in days since the epoch of the first light (MJD 58206.00) is in the rest frame.
[a] From applying the Arnett (1982) model to the light curves of SN 2018aoz, as typically done for radioactively powered SNe (e.g., Drout et al. 2016; Li et al. 2019), approximating the ^{56}Ni-dominated opacity in the photospheric phase as $\kappa \sim 0.1\,\mathrm{cm^2\,g^{-1}}$ (Paper I).
[b] From He-shell DDet simulations (Paper I).

5.3. Ejecta Interaction with CSM

The interaction between the SN ejecta and CSM near the progenitor can produce excess emission with properties dependent on the mass and spatial distribution of the CSM. We model the early light curves of SN 2018aoz as a combination of a power-law (for the underlying SN emission) and ejecta-CSM interaction emission (for the infant-phase excess emission), adopting the model of (Piro 2015, P15, hereafter) for the latter. Here, we describe the CSM model and geometries (Section 5.3.1) considered, and then discuss the results in the context of both H-poor (Section 5.3.2) and H-rich CSM (Section 5.3.3).

5.3.1. Model Description

The observed interaction emission is largely determined by properties of the outermost CSM layer (Nakar & Piro 2014; Piro 2015), represented as a uniform-density and spherically symmetric envelope with mass $M_{\rm env}$ and radius $R_{\rm env}$ in the P15 model. The luminosity ($L_{\rm CSM}$) is provided by the following equation determined by $M_{\rm env}$, $R_{\rm env}$, ejecta mass ($M_{\rm ej}$), ejecta kinetic energy ($E_{\rm ej}$), and opacity (κ):

$$L_{\rm CSM}(t) = \frac{t_{\rm env}E_{\rm env}}{t_p^2}\exp\left[-\frac{t(t+2t_{\rm env})}{2t_p^2}\right], \quad (6)$$

where $t_{\rm env} \propto E_{\rm ej}^{-0.5}M_{\rm ej}^{0.35}M_{\rm env}^{0.15}R_{\rm env}$ is the envelope expansion timescale post-explosion, $E_{\rm env} \propto E_{\rm ej}M_{\rm ej}^{0.7}M_{\rm env}^{-0.7}$ is the total energy transferred from the ejecta to the envelope, $t_p \propto \kappa^{0.5}E_{\rm ej}^{-0.25}M_{\rm ej}^{0.17}M_{\rm env}^{0.57}$ is the emission peak epoch, and t is the time in seconds since the explosion epoch (t_0). Adopting a blackbody for the spectral energy distribution of the interaction emission, the blackbody temperature follows

$$T_{\rm CSM}(t) = \left[\frac{L_{\rm CSM}(t)}{4\pi\sigma_{\rm SB}(R_{\rm env}+v_{\rm env}t)^2}\right]^{1/4}, \quad (7)$$

where $v_{\rm env} \propto E_{\rm ej}^{-0.5}M_{\rm ej}^{0.35}M_{\rm env}^{0.15}$ is the envelope expansion velocity post-explosion.

We also consider ejecta interaction with CSM distributed in an equatorially concentrated disk or torus as follows. Such CSM may divert the flow of SN ejecta away from the equatorial plane, where it obscures the ejecta-CSM interaction from viewing angles (θ) above and below the equatorial plane ($\theta = 0°$). Note that similar obscuration is expected for ejecta-companion interaction due to the diverted flow of SN ejecta around the companion (Kasen 2010), resulting in attenuated brightness of the interaction as described by Equation (1) for viewing angles θ away from the binary axis toward the companion ($\theta = 0°$ in Equation (1)). We approximate the attenuation of ejecta-CSM interaction brightness for a viewing angle θ above or below the equatorial plane as similar to that of ejecta-companion interaction for the same angle θ away from the binary axis toward the companion for a distant observer, assuming a similar flow of SN ejecta away from the interaction region. The brightness of ejecta interaction with equatorially concentrated CSM would thus be $L_{\rm CSM} \times S(\theta)$ for θ ranging from the equatorial plane (0°) to the poles (90°), using $S(\theta)$ from Equation (1). $S(0°) = 1.0$ means the brightness along the equatorial plane is identical to the case of spherically symmetric CSM, $L_{\rm CSM}$, while $\theta = 90°$ provides the minimum observed brightness of $L_{\rm CSM} \times 0.45$.

5.3.2. CSM from a WD or He-star Companion

We primarily consider the case of H-poor CSM originating from a WD or He-star companion, using the electron scattering opacity of $\kappa = 0.2\,{\rm cm^2\,g^{-1}}$, since those are the most likely companions for SN 2018aoz based on the constraints derived from the early light curves (Section 4) and nebular-phase spectra (Section 6.3). In this case, the SN explosion could occur after the merger of the binary or during an earlier stage of binary mass transfer (Shen 2015). The distribution of CSM initially after the merger and during earlier stages of mass transfer is expected to be equatorially concentrated, rather than spherically symmetric as assumed in P15, though the distribution can evolve toward spherical symmetry on a timescale of hours after the merger (Guillochon et al. 2010; Schwab et al. 2012; Pakmor et al. 2013).

Table 4 presents the best-fit parameters obtained by fitting the early light curves of SN 2018aoz during 0–8 days since the first light, excluding the B-band light curve during 0–1 day, using two extreme cases of viewing angles, $\theta = 0°$ (equal to the spherically symmetric case) and $\theta = 90°$, and two cases of relatively small and large ejecta masses and kinetic energies for SN 2018aoz following Section 5.2. Note that the reduced χ-squared statistics of the four cases are nearly identical ($\chi^2_{\rm R} \sim 3.3$), indicating that the goodness of fit is very similar for the different cases. For the properties of the early excess emission in the fit, we allowed for ranges of $M_{\rm env}$ in 10^{-5}–$10^{-2}\,M_\odot$ and $R_{\rm env}$ in 10^9–10^{13} cm that easily accommodate the obtained fit parameters. Figure 10 compares the light and color curves of the best-fit ejecta-CSM interaction model obtained in the case of $M_{\rm ej} = 0.80\,M_\odot$, $E_{\rm ej} = 0.63 \times 10^{51}$ erg, and $\theta = 0°$ (red-dashed curves) to those of SN 2018aoz and the two other best-fit models of surface ^{56}Ni heating (Section 5.1) and ejecta-companion interaction (Section 5.2), where the goodness of fit is very similar for the three models. As can be seen in the table, the difference of $t_{\rm PL}$–$t_0 \sim 0.22$–0.26 day obtained for the ejecta-CSM interaction model is near the lower extreme of the range obtained for the surface ^{56}Ni heating (0.54 day) and ejecta-companion interaction (0.28–0.60 day) models, consistent with there being a delay (or dark phase) of $\lesssim$1 day between the explosion and the onset of the power-law rise in SN 2018aoz (Paper I).

We examine whether the CSM mass, $M_{\rm env}$, required to fit the observed infant-phase excess emission is compatible with the expectations of CSM after a merger (or *post-merger CSM*). The total CSM mass ($M_{\rm CSM}$) is not necessarily equal to $M_{\rm env}$ since the envelope represents only the outermost layer of CSM near $R_{\rm env}$ that dominates the ejecta-CSM interaction emission. $M_{\rm CSM} \gtrsim M_{\rm env}$ in general, where $M_{\rm CSM} = M_{\rm env}$ is for the case of entirely uniform-density CSM, and $M_{\rm CSM}/M_{\rm env}$ increases with the central concentration of the CSM density distribution. Adopting a $\rho \propto r^{-3}$ density distribution expected for post-merger CSM (Piro & Morozova 2016), we obtain the following equation for $M_{\rm CSM}$ in terms of $M_{\rm env}$ and $R_{\rm env}$:

$$M_{\rm CSM} \simeq 4\pi R_{\rm env}^3\rho_{\rm env}\log(R_{\rm env}/R_*), \quad (8)$$

where $\rho_{\rm env} = 3M_{\rm env}/4\pi R_{\rm env}^3$ is the CSM density in the outermost layer (= envelope density) and R_* is the progenitor radius. R_* is taken to be $\sim 6 \times 10^8$ cm, the expected shock breakout radius of SN 2018aoz (Section 5.4).

Table 4, Column 5, provides the derived CSM properties of $\rho_{\rm env}$ and $M_{\rm CSM}$ that would be implied by the fit parameters using Equation (8). Overall, these properties appear to be

Table 4
Ejecta-CSM Interaction Model Fit Parameters for H-poor CSM ($\kappa = 0.2\ \mathrm{cm^2\ g^{-1}}$)

$M_{\rm ej}$ and $E_{\rm ej}$[a]	Viewing Angle	Fit Parameters	$\chi^2_{\rm R}$	CSM Properties
$0.80\ M_\odot$ and 0.63×10^{51} erg	$\theta = 0°$	$M_{\rm env} = 2.0 \times 10^{-3}\ M_\odot$ $R_{\rm env} = 3.5 \times 10^9$ cm $t_0 = -0.04$ day $t_{\rm PL} = 0.19$ day $\alpha_{B,V,i} = (2.12, 1.81, 2.14)$	3.29	$\rho_{\rm env} = 22\ \mathrm{g\ cm^{-3}}$ $M_{\rm CSM}\ (\rho \propto r^{-3}) = 0.0046\ M_\odot$
	$\theta = 90°$	$M_{\rm env} = 1.7 \times 10^{-3}\ M_\odot$ $R_{\rm env} = 1.2 \times 10^{10}$ cm $t_0 = -0.06$ day $t_{\rm PL} = 0.19$ day $\alpha_{B,V,i} = (2.12, 1.82, 2.14)$	3.29	$\rho_{\rm env} = 0.47\ \mathrm{g\ cm^{-3}}$ $M_{\rm CSM}\ (\rho \propto r^{-3}) = 0.0065\ M_\odot$
$1.05\ M_\odot$ and 0.82×10^{51} erg	$\theta = 0°$	$M_{\rm env} = 2.1 \times 10^{-3}\ M_\odot$ $R_{\rm env} = 3.1 \times 10^9$ cm $t_0 = -0.03$ day $t_{\rm PL} = 0.19$ day $\alpha_{B,V,i} = (2.12, 1.81, 2.14)$	3.29	$\rho_{\rm env} = 34\ \mathrm{g\ cm^{-3}}$ $M_{\rm CSM}\ (\rho \propto r^{-3}) = 0.0045\ M_\odot$
	$\theta = 90°$	$M_{\rm env} = 1.7 \times 10^{-3}\ M_\odot$ $R_{\rm env} = 1.1 \times 10^{10}$ cm $t_0 = -0.06$ day $t_{\rm PL} = 0.20$ day $\alpha_{B,V,i} = (2.12, 1.82, 2.14)$	3.29	$\rho_{\rm env} = 0.61\ \mathrm{g\ cm^{-3}}$ $M_{\rm CSM}\ (\rho \propto r^{-3}) = 0.0065\ M_\odot$

Note. t_0 and $t_{\rm PL}$ are in days since the epoch of the first light (MJD 58206.00) is in the rest frame.
[a] The two cases of $M_{\rm ej}$ and $E_{\rm ej}$ are the same as the ones used for the ejecta-companion interaction in Table 3.

incompatible with the theoretical expectations for post-merger CSM. In simulations of a violent merger, the post-merger CSM mass can be $\sim$0.1–0.7 $M_\odot$ depending on the companion mass (Dan et al. 2014), which is much larger than the $M_{\rm CSM} \lesssim 0.007\ M_\odot$ required to fit the observed infant-phase excess emission. The post-merger CSM radius is also expected to expand on short timescales, beginning from $\sim 10^{10}$ cm during the merger and expanding to $\sim 10^{11}$ cm in only a few hours after the merger (Piro & Morozova 2016), becoming less compatible with the fitted CSM radii of $R_{\rm env} \lesssim 10^{10}$ cm on the timescale of the infant-phase excess emission. Thus, the emission is not likely to be from post-merger CSM.

We instead consider CSM of smaller mass and radius expected in *premerger* stages of binary mass transfer, before the WD or He-star companion is disrupted, for the origin of the infant-phase excess emission. For example, in simulations of He-shell DDets from WD-WD mergers, $\lesssim 0.1\ M_\odot$ of CSM is expected to be present at the time of the explosion, which occurs before the merger is completed, distributed in a torus around the progenitor star. The outermost layers of the torus are located at $\gtrsim 10^9$ cm where the CSM density is expected to be $\lesssim 10^3\ \mathrm{g\ cm^{-3}}$ (Guillochon et al. 2010; Pakmor et al. 2013). These premerger CSM properties are comparable to $R_{\rm env} = (3.1\text{–}3.5) \times 10^9$ cm and $\rho_{\rm env} = 22\text{–}34\ \mathrm{g\ cm^{-3}}$ obtained for the cases with $\theta = 0°$ viewing angle (see Table 4). If the premerger CSM density distribution is similar to the post-merger case ($\rho \propto r^{-3}$), then the corresponding total CSM mass of $M_{\rm CSM} \sim 0.005\ M_\odot$ is relatively small compared to the CSM masses expected in He-shell DDet simulations ($\sim$0.05–0.10 $M_\odot$; Guillochon et al. 2010). However, since $M_{\rm CSM}$ can be larger for steeper premerger CSM density distributions, ejecta interaction with premerger CSM remains possible for the origin of the observed infant-phase excess emission in SN 2018aoz.

5.3.3. CSM from a Main-sequence or Subgiant Companion

For the less likely case of a few solar mass main-sequence or subgiant companions in SN 2018aoz (Section 4), we briefly consider the possibility of ejecta interaction with solar-composition CSM from such companions, adopting the electron scattering opacity of $\kappa = 0.34\ \mathrm{cm^2\ g^{-1}}$. Since those companions are mainly expected to trigger Type Ia SNe via accretion (Maoz et al. 2014), the CSM is likely to be an equatorially concentrated disk or toroid. Table 5 shows the best-fit parameters obtained by fitting the early light curves of SN 2018aoz using the aforementioned two extreme cases of viewing angles for equatorially concentrated CSM, $\theta = 0°$ for the equatorial viewing angle, and 90° for the polar viewing angle, and two cases of relatively small and large ejecta masses and kinetic energies for SN 2018aoz. For uniform-density CSM, the total CSM mass is expected to be $M_{\rm CSM} = M_{\rm env}$, ranging from 0.0011–0.0014 $M_\odot$, while the total CSM mass expected for the relatively steep CSM density distribution of $\rho \propto r^{-3}$ ranges from 0.0035–0.0046 $M_\odot$ (Table 5, Column 5, based on Equation (8)). Overall, if SN 2018aoz was triggered by accretion from a few solar mass main-sequence or subgiant companion, then the observed infant-phase excess emission can be produced by ejecta interaction with an $\sim$0.001–0.005 $M_\odot$ accretion disk near $\sim(4\text{–}14) \times 10^9$ cm.

5.4. Search for Shock Breakout

Shock breakout is expected to occur shortly after an SN explosion when the outgoing shock wave breaks through the surface of the progenitor star (Nakar & Sari 2010; Piro et al. 2010). Early observations of Type Ia SNe have been used to search for evidence of shock breakout based on the expected thermal emission from the shock-heated envelope. However, since the luminosity of the shock breakout emission scales with the radius of the progenitor star, this emission has not yet been

Table 5
Ejecta-CSM Interaction Model Fit Parameters for Solar-composition CSM ($\kappa = 0.34$ cm^2 g^{-1})

$M_{\rm ej}$ and $E_{\rm ej}$[a]	Viewing Angle	Fit Parameters	$\chi^2_{\rm R}$	CSM Properties
0.80 $M_\odot$ and 0.63 $\times$ 10^{51} erg	$\theta = 0°$	$M_{\rm env} = 1.3 \times 10^{-3}\ M_\odot$ $R_{\rm env} = 4.9 \times 10^9$ cm $t_0 = -0.03$ day $t_{\rm PL} = 0.19$ day $\alpha_{B,V,i} = (2.12, 1.81, 2.14)$	3.30	$\rho_{\rm env} = 5.3$ g cm^{-3} $M_{\rm CSM}$ ($\rho \propto r^{-3}$) = 0.0035 $M_\odot$
	$\theta = 90°$	$M_{\rm env} = 1.1 \times 10^{-3}\ M_\odot$ $R_{\rm env} = 1.4 \times 10^{10}$ cm $t_0 = -0.05$ day $t_{\rm PL} = 0.20$ day $\alpha_{B,V,i} = (2.12, 1.82, 2.14)$	3.28	$\rho_{\rm env} = 0.19$ g cm^{-3} $M_{\rm CSM}$ ($\rho \propto r^{-3}$) = 0.0045 $M_\odot$
1.05 $M_\odot$ and 0.82 $\times$ 10^{51} erg	$\theta = 0°$	$M_{\rm env} = 1.4 \times 10^{-3}\ M_\odot$ $R_{\rm env} = 4.4 \times 10^9$ cm $t_0 = -0.03$ day $t_{\rm PL} = 0.19$ day $\alpha_{B,V,i} = (2.12, 1.81, 2.14)$	3.30	$\rho_{\rm env} = 7.8$ g cm^{-3} $M_{\rm CSM}$ ($\rho \propto r^{-3}$) = 0.0035 $M_\odot$
	$\theta = 90°$	$M_{\rm env} = 1.2 \times 10^{-3}\ M_\odot$ $R_{\rm env} = 1.2 \times 10^{10}$ cm $t_0 = -0.05$ day $t_{\rm PL} = 0.20$ day $\alpha_{B,V,i} = (2.12, 1.82, 2.14)$	3.28	$\rho_{\rm env} = 0.33$ g cm^{-3} $M_{\rm CSM}$ ($\rho \propto r^{-3}$) = 0.0046 $M_\odot$

Note. t_0 and $t_{\rm PL}$ are in days since the epoch of the first light (MJD 58206.00) is in the rest frame.
[a] The two cases of $M_{\rm ej}$ and $E_{\rm ej}$ are the same as the ones used for the ejecta-companion interaction in Table 3.

observed in Type Ia SNe due to the small size of WDs. The non-detection of shock breakout emission in early Type Ia SNe has been used to constrain the radius of the SN progenitor, e.g., in the case of SN 2011fe to be $\lesssim$0.02 $R_\odot$ (Bloom et al. 2012).

We investigate the origin of the infant-phase excess emission by comparing the observed early light curves of SN 2018aoz with what is expected from shock breakout emission. Adopting the model of Piro et al. (2010), which assumes an approximately spherically symmetric explosion and a radial shock acceleration law, the shock breakout emission luminosity ($L_{\rm SBO}$) and temperature ($T_{\rm SBO}$) are determined by the ejecta mass ($M_{\rm ej}$) and the radius of the progenitor star at the time of shock breakout ($R_{\rm SBO}$) as follows:

$$L_{\rm SBO}(t) = 7^{-4/3} \times 2 \times 10^{40} (g_9/K_{13})^{-0.41} \times V_9^{1.9} \rho_6^{0.36} R_{8.5}^{0.83} t_4^{-0.16}\ {\rm erg\ s^{-1}}, \quad (9)$$

$$T_{\rm SBO}(t) = 7^{-1/3} \times 2 \times 10^{4} (g_9/K_{13})^{-0.058} \times V_9^{0.030} \rho_6^{0.0058} R_{8.5}^{0.11} t_4^{-0.44}\ {\rm K}, \quad (10)$$

where the first terms are correction factors to fix the improper scalings (Bloom et al. 2012), $g_9 \propto M_{\rm ej}/R_{\rm SBO}^2$ represents surface gravity, $K_{13} = K/(10^{13}\ {\rm cgs})$ represents the nonrelativistic degenerate equation of state constant (K) with $\mu_e \sim 2$ for C + O WDs, $V_9 \sim 0.6$ and $\rho_6 \sim 2 g_9^{0.11}$ represent the shock velocity and density, respectively, $R_{8.5} = R_{\rm SBO}/(10^{8.5}\ {\rm cm})$ and $t_4 = (t - t_0)/(10^4\ {\rm s})$ represents the time since the epoch of the explosion (t_0).

We fit the early light curves of SN 2018aoz during 0–8 days since the first light (excluding the B-band light curve during 0–1 day) as a combination of power-law (for the underlying SN emission) and shock breakout emission (for the infant-phase excess emission). The best-fit shock breakout radius is $R_{\rm SBO}$ = (3.5–3.7) $\times 10^9$ cm, or 0.050–0.053 $R_\odot$, where the lower and upper limits of the range represent the results obtained using two cases of relatively small and large values of $M_{\rm ej}$ (= 0.80 and 1.05 $M_\odot$), respectively, for SN 2018aoz following the methods of Sections 5.2 and 5.3.

This range of fitted $R_{\rm SBO}$ is larger than the $R_{\rm SBO}$ that can be reasonably expected for the progenitor of SN 2018aoz, indicating that shock breakout is unlikely to be the origin of the observed infant-phase excess emission. For a typical C+O WD with mass of $\sim$1.0 $M_\odot$, the shock breakout radius after the possible expansion due to a deflagration phase is expected to be $\sim 6 \times 10^8$ cm (Piro et al. 2010). While explosion asymmetry can lead to a factor of $\lesssim$2 difference in the inferred $R_{\rm SBO}$, corresponding to the expected range of angular variation of shock breakout luminosity for a compact progenitor (Afsariardchi & Matzner 2018), an unreasonably intense deflagration phase is still required to achieve such a large radius as the fitted $R_{\rm SBO} = (3.5–3.7) \times 10^9$ cm. Moreover, explosion mechanisms dominated by deflagration typically leave substantial amounts of unburnt carbon (Nomoto et al. 1984), while no C spectral features are seen in SN 2018aoz (Section 7.5). For the case of a He-shell DDet origin, which lacks a deflagration phase, the radius of the best-fit He-shell DDet model progenitor for SN 2018aoz—a 1.05 $M_\odot$ C + O WD with a 0.01 $M_\odot$ He shell—is only 5.14×10^8 cm (Paper I). In this case, while the He shell can generally be expected to undergo some shock-driven expansion during the He-shell DDet process, the fitted $R_{\rm SBO}$ of (3.5–3.7) $\times 10^9$ cm is unrealistic for the best-fit He-shell DDet model progenitor due to the extremely small He-shell mass.

6. Nebular-phase Evolution: Constraints on the Progenitor System and Explosion Mechanism

6.1. Nebular-phase Light Curves

Figure 1 compares the evolution of SN 2018aoz light curves in the BVi (blue, green, and red circles) bands from the

Table 6
Nebular-phase Broad Emission Line Fluxes

Phase[a]	[Fe III] λ 4658 Å (10^{-14} erg s^{-1} cm^{-2})	[Co III] λ 5888 Å (10^{-14} erg s^{-1} cm^{-2})	[Fe II] + [Ni II] λ 7155 Å, 7378 Å (10^{-14} erg s^{-1} cm^{-2})	7290 Å/[Fe III][b]
+259.4	10.934 ± 0.010	1.347 ± 0.003	1.710 ± 0.003	0.1564 ± 0.0003
+277.3	N/A	1.029 ± 0.003	1.443 ± 0.002	N/A
+296.4	7.629 ± 0.009	0.632 ± 0.003	1.086 ± 0.002	0.1424 ± 0.0003
+382.5	2.658 ± 0.005	0.245 ± 0.002	0.580 ± 0.002	0.2181 ± 0.0008

Notes.
[a] Phases are measured in observer frame days since the *B*-band maximum.
[b] The ratio of the flux of the 7290 Å feature to that of [Fe III] (Polin et al. 2021).

beginning to the nebular phase with those of normal Type Ia SN 2011fe (dashed lines; Munari et al. 2013; Tsvetkov et al. 2013) that have been scaled to match the peak absolute magnitude, $M_B = -19.32$ mag, and post-peak decline rate, $\Delta M_{15}(B) = 1.12$ mag, of SN 2018aoz. The light curves of SNe 2018aoz and 2011fe show a good agreement overall throughout their evolution, especially in the *B* band, confirming that the evolution of SN 2018aoz in the nebular phase continues to match those of normal Type Ia SNe. The nebular-phase light curves of SN 2018aoz decline linearly at rates of 0.0131 ± 0.0001, 0.0129 ± 0.0001, and 0.0083 ± 0.0003 mag day^{-1} in the *B*, *V*, and *i* bands, respectively, with a *BVi*-averaged decline rate of 0.0127 mag day^{-1}. For comparison, we measure the light-curve decline rates of SN 2011fe during the nebular phase to be 0.0134, 0.0138, and 0.0099 mag day^{-1} in the *B*, *V*, and *i* bands, respectively.

6.2. Nebular-phase Spectra

Figure 2 shows the identification of nebular-phase [Fe III] λ4658 Å and [Co III] λ5888 Å features in SN 2018aoz (red and green vertical regions, respectively), whose flux ratio is associated with the evolution of ^{56}Ni → ^{56}Co → ^{56}Fe radioactive decay in Type Ia SNe (Kuchner et al. 1994), as well as that of a double-peak feature near 7290 Å (blue vertical region). The nebular-phase 7290 Å feature of Type Ia SNe can be from the [Ca II] λ7291, 7323 Å doublet, [Fe II] λ7155 Å, [Ni II] λ7378 Å, or some combination thereof (Flörs et al. 2020; Polin et al. 2021). The double-peak 7290 Å feature observed in SN 2018aoz, as well as most normal events (e.g., SN 2011fe; Mazzali et al. 2015), is most likely dominated by [Fe II] and [Ni II] emission since the [Ca II] feature would not be resolved as a doublet at typical Type Ia SN velocities (Polin et al. 2021). For each of the four nebular-phase spectra of SN 2018aoz, Table 6 provides the measured fluxes of [Fe III], [Co III], and the 7290 Å feature ([Fe II] + [Ni II]), as well as the ratios between the fluxes of the 7290 Å feature to those of [Fe III] λ4658 Å, called 7290 Å/[Fe III] hereafter. To obtain uncertainties in the fluxes, we estimated noise levels by smoothing each spectrum with a second-order Savitsky–Golay filter with a width of 150 Å, which is $\lesssim$1/4 of the feature widths. The average 7290 Å/[Fe III] ratio of 0.149 ± 0.007 between 120 and 320 days since the peak for SN 2018aoz is near the lower extreme of what has been found in normal Type Ia SNe in the range of ∼0.1–1.0 (Polin et al. 2021).

[43] The *I*-band magnitudes of SN 2011fe were converted to the *i* band by subtracting $-2.5 \log_{10}(3631 \text{ Jy}/2416 \text{ Jy})$.

Figure 2 also shows the expected positions of narrow emission lines of H, He, and O near Hα λ6563 Å, He I λ5875, 6678 Å, and [O I] λ6300, 6364 Å, respectively. In Type Ia SNe, these low-velocity lines may be produced by swept-up material from the companion (e.g., Kollmeier et al. 2019) or CSM, including disrupted companion material following a violent merger (Kromer et al. 2013; Mazzali et al. 2022; Tucker et al. 2022). All of the lines appear to be absent in SN 2018aoz, similar to most other Type Ia SNe (Mattila et al. 2005; Leonard 2007; Shappee et al. 2013; Maguire et al. 2016; Tucker et al. 2020), which argues against the presence of a substantial amount of swept-up material (see below). By injecting synthetic emission lines of H and He with an FWHM = 1000 km s^{-1} into the observed nebular spectra, modeling Doppler shifts from the rest-frame wavelength of up to $\pm$1000 km s^{-1}, and estimating the rms of the local spectral region following the methods of Sand et al. (2018b, 2019), we find 3σ flux upper limits for the Hα and He I lines. We do the same for [O I], but using an FWHM = 2000 km s^{-1} and up to $\pm$2000 km s^{-1} Doppler shifts that can be expected for [O I] (Taubenberger et al. 2013). Table 7 presents the measured upper limits and their corresponding luminosities.

6.3. Constraints on the Nondegenerate Companion and CSM

We now place constraints on the presence of a nondegenerate companion or CSM from the violent merger case of double degeneracy in the progenitor of SN 2018aoz based on the absence of predicted emission lines from their unburned swept-up material in the observed nebular-phase spectra. The ejecta of Type Ia SNe are expected to strip/ablate ∼0.1 $M_\odot$ of H- or He-rich materials from a nondegenerate companion (e.g., Botyanszki et al. 2018), while in the case of a violent merger, ∼0.1–0.7 $M_\odot$ of H-poor CSM composed of O or He can be expected depending on the mass and composition of the companion WD (Dan et al. 2014). Multiple spectral synthesis studies have shown that even trace amounts ($\sim 10^{-3}$ $M_\odot$) of low-velocity H will lead to observable nebular-phase Hα emission (Mattila et al. 2005; Botyanszki et al. 2018; Dessart et al. 2020). For H-poor material, some recent studies (Dessart et al. 2020) find that $\lesssim$0.2 $M_\odot$ of O or He could be hidden by metal line-blanketing while other studies find that even very small amounts, ∼0.05 $M_\odot$ of O (Mazzali et al. 2022) or $\sim 10^{-3}$ $M_\odot$ of He (Botyanszki et al. 2018), would be observable.

In Columns 5 and 6 of Table 7, we use the models of Botyanszki et al. (2018) and Dessart et al. (2020), respectively, to obtain upper limits on the masses of low-velocity H and He based on the observed upper limits on the luminosities of their

Table 7
Nebular-phase Emission Line Flux and Luminosity Limits

Line	Phase[a]	Flux Limit (10^{-17} erg s^{-1} cm^{-2})	Luminosity Limit (10^{36} erg s^{-1})	Mass Limit[b] (10^{-4} $M_\odot$)	Mass Limit[c] (10^{-4} $M_\odot$)
Hα λ6563 Å	+259.4	5.4	3.2	4	10–16
	+277.3	5.0	3.0	4	12–18
	+296.4	6.3	3.8	5	16–24
	+382.5	7.7	4.6	9	100–130
He I λ5875 Å	+259.4	10.0	6.0	25	
	+277.3	7.8	4.7	25	
	+296.4	9.0	5.4	33	
	+382.5	17.6	10.5	104	
He I λ6678 Å	+259.4	5.4	3.2	18	
	+277.3	6.7	4.0	25	
	+296.4	10.5	6.3	43	
	+382.5	7.7	4.6	55	
[O I] λ6300 Å	+259.4	16.9	10.1		
	+277.3	17.6	10.5		
	+296.4	21.6	13.0		
	+382.5	25.8	15.5		
[O I] λ6364 Å	+259.4	16.9	10.1		
	+277.3	21.1	12.6		
	+296.4	21.6	13.0		
	+382.5	25.8	15.5		

Note. All implanted lines have peak fluxes corresponding to 3 times the local rms with an FWHM = 1000 km s^{-1}, except for the He I λ5875 Å line, where we used a peak flux of 4 times the local rms. We infer upper limits on the mass of the emitting elements based on the luminosity limits and the model predictions of Botyanszki et al. (2018)[b] and Dessart et al. (2020)[c].
[a] Phases are measured in observer frame days since the *B*-band maximum.

lines. The range of values in Column 6 correspond to the range of mass upper limits derived for the set of delayed detonation as well as sub-Chandrasekhar-mass explosion models from Dessart et al. (2020). As seen in the columns, even the most conservative upper limits on H and He masses in SN 2018aoz permit less than 1.3 $\times 10^{-2}$ and 1.0 $\times 10^{-2}$ $M_\odot$ of each, respectively, making the presence of even a trace amount of H extremely unlikely, as supported by both models, while Botyanszki et al. (2018) would also exclude the presence of significant He. Overall, the nebular-phase spectra of SN 2018aoz disfavor the presence of a nondegenerate companion, and to a lesser extent, the large mass of H-poor CSM expected from a violent merger. The presence of a main-sequence or RG companion is especially disfavored by the H constraints based on both Botyanszki et al. (2018) and Dessart et al. (2020), while the He constraints based on Botyanszki et al. (2018) would even disfavor a naked He-star companion.

6.4. Constraints on Sub-Chandrasekhar-mass and Asymmetric Explosion Mechanisms

Nebular-phase spectra of Type Ia SNe can also offer constraints on the explosion mechanism and geometry. In particular, the strength of [Ca II] emission near 7290 Å can be linked to the mass of the progenitor WD. Pure detonations of low-mass WDs are expected to undergo incomplete burning due to their lower density (Polin et al. 2021), leading to the production of Ca mixed with other Fe-peak elements, which then cool efficiently via [Ca II] in the nebular phase (Hoeflich et al. 2021; Polin et al. 2021). As explained above, the double-peak 7290 Å features seen in SN 2018aoz and most normal Type Ia SNe (e.g., SN 2011fe) are likely dominated by [Fe II] and [Ni II], indicating weak [Ca II] emission. This may imply the explosion of a relatively massive WD. For instance, a 1.26 $M_\odot$ WD explosion can produce weak and double-peaked emission near 7290 Å as seen in SN 2011fe (Mazzali et al. 2015). Comparisons to the models of Polin et al. (2021) also support a $\gtrsim$1.2 $M_\odot$ WD explosion for the weak emission seen in SN 2018aoz (see Figure 14). In this case, however, reconciling the relatively large total mass with the estimated ejecta mass of SN 2018aoz based on 1D modeling of its fast-rising light curves (0.8–1.05 $M_\odot$; Paper I) may rely on viewing angle effects and explosion asymmetry, which can be caused by tidal heating or a surface He-shell detonation (Iben & Tutukov 1994; Iben et al. 1998).

Such an explosion asymmetry may leave imprints on other lines in the nebular phase. In particular, the [Fe II] λ7155 Å and [Ni II] λ7378 Å emission features seen in normal Type Ia SNe are expected to be Doppler shifted as a result of the motion of the ejecta core in an asymmetric explosion mechanism (Maeda et al. 2010b, 2010c; Li et al. 2021). Note that these two emission features are dominated by single line transitions (with a minor contribution from the weak [Fe II] λ7171 Å line), whereas other emission features of Fe-peak elements, including [Fe III] and [Co III], have contributions from a blend of broad absorption features with wavelength separations smaller than their typical line widths (Maeda et al. 2010b; Flörs et al. 2020). Thus, shifts in the central wavelengths of [Fe III] and [Co III] are not solely attributable to Doppler velocity. Figure 11 shows that the peak wavelengths of the observed [Fe II] and [Ni II] features are blueshifted in the nebular-phase spectra of SN 2018aoz, corresponding to average velocities of (-2.3 ± 0.3) and (-1.6 ± 0.7) $\times 10^3$ km s^{-1}, respectively. These are among the most blueshifted velocities reported for those features in Type Ia SNe (Maeda et al. 2010c; Li et al. 2021). For both asymmetric Chandrasekhar-mass explosion mechanisms (Maeda et al. 2010b) and DDets (Boos et al. 2021), the observed velocities of Fe and Ni in SN 2018aoz point to a viewing angle where the primary component of the ejecta core is approaching the observer. However, we note that asymmetric explosions only provide faster-rising light curves from viewing angles where the ejecta core is *receding* from the observer (see Boos et al. 2021; Shen et al. 2021b) since those directions provide higher ejecta velocities and lower densities, which leads to shorter diffusion times. Thus, asymmetric effects alone are unable to reconcile the fast-rising light curves with a relatively large total ejecta mass. We discuss possible explanations for these features in Section 8.3.

7. Comparison to the He-shell DDet Models

The *B*-band plateau and rapid redward $B - V$ color evolution of SN 2018aoz within the first $\sim$1 day post-explosion have been attributed to the presence of an over-density of Fe-peak elements in the outer 1% of the SN-ejected mass (Paper I). In addition, the relatively short 15.3-day rise time of SN 2018aoz among normal Type Ia SNe indicates that SN 2018aoz either (1) was a spherically symmetric explosion with a total ejecta mass of $\sim$0.8–1.0 $M_\odot$, which is significantly smaller than the

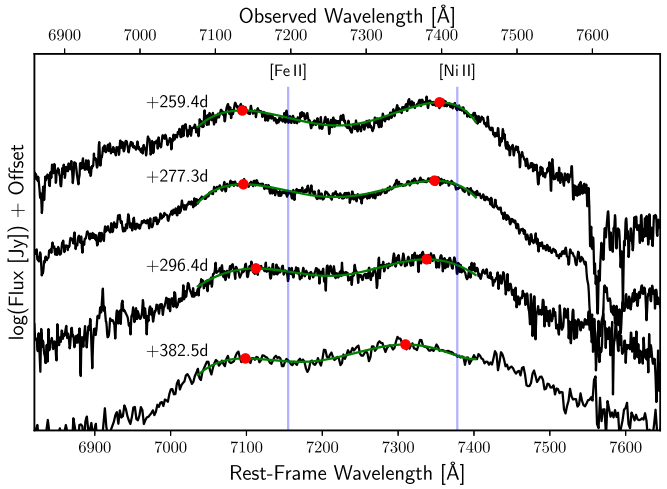

Figure 11. The dereddened nebular-phase spectra of SN 2018aoz (black) zoomed in on the [Fe II] and [Ni II] features whose rest-frame wavelengths are indicated with blue vertical lines. The red circles are the peaks of the emission features obtained by fitting polynomials ($n = 12$; green curves) to the spectra.

Chandrasekhar mass of $\sim$1.4 $M_\odot$, or (2) was an asymmetric explosion. Among the proposed explanations for the distribution of Fe-peak elements in the outer ejecta of SN 2018aoz—off-center deflagration, gravitationally confined detonation, and He-shell DDet—only He-shell DDet is compatible with a sub-Chandrasekhar total ejecta mass (Kromer et al. 2010; Woosley & Kasen 2011; Polin et al. 2019). Below we examine the compatibility between the other observed properties of SN 2018aoz and a set of 1D He-shell DDet model predictions.

7.1. He-shell DDet Simulations

For our comparisons, we primarily use the set of thin He-shell DDet models from Paper I with core C + O WD and He-shell masses ranging from 1.00–1.10 and 0.01–0.012 $M_\odot$, respectively, created following the methods of Polin et al. (2019). The modeling process involves two stages. First, we perform hydrodynamic simulations with full nucleosynthesis using Castro, a compressible hydrodynamics code built on the AMReX framework (Almgren et al. 2010; Zingale et al. 2018). After the SN ejecta has reached homologous expansion we perform radiative transport calculations with Sedona (Kasen et al. 2006) in order to produce synthetic light curves and spectra of our models. The only way our methods differ from the Polin et al. (2019) study is that we begin our radiative transport simulations earlier than the previously published models (beginning at 0.1 day instead of 0.25 day) in order to model the natal epochs observed in SN 2018aoz. In Paper I, we found that the model with a 1.05 $M_\odot$ WD + 0.01 $M_\odot$ He shell provided the best fit to the early (0–8 days since the first light) $B-V$ color and near-peak BVi luminosity evolution of SN 2018aoz. Here, we provide an expanded comparison between these models and both the infant-phase and near-peak properties of the SN. We supplement these with comparisons to the predictions for the nebular-phase emission line ratios of the sub-Chandrasekhar-mass He-shell DDet models from Polin et al. (2021).

7.2. Comparison to Infant-phase Evolution

Figure 12 compares the observed early color and light curves (filled black circles) of SN 2018aoz with those (colored curves) predicted by the He-shell DDet models during the first 5 days. As noted in Paper I, the 1.05 $M_\odot$ WD + 0.010 $M_\odot$ He-shell model (magenta curves) provides the best fit to the early $B-V$ color evolution of SN 2018aoz, including the timing and magnitude of the rapidly evolving NRB-phase color. All of the models, on the other hand, poorly fit the observed $V-i$ color, significantly overpredicting the amount of reddening observed. This discrepancy could be due to either (1) a line effect, such as differences in the modeled and observed strength of Ca II features in the I band around 8000 Å due to Ca produced by the initial He-shell detonation (Polin et al. 2021), or (2) a continuum effect, such as differences in the color temperature that are influenced by the radioactive heating rate (Section 8.5).

In addition, none of the current suites of models can fit the early light curves entirely during the first 5 days (right panels), although some can reproduce the observed light-curve evolution of the SN at various phases. From 0.5 day onward, the cyan and magenta models (1.10 and 1.05 $M_\odot$ WDs with 0.010 $M_\odot$ He shells) provide the best fits, although both models significantly underpredict the observed luminosity over the earliest $\lesssim$0.5 day. On the one hand, as noted in Paper I, it is only necessary to add an additional 1.1 $\times 10^{-3}$ $M_\odot$ of He to the best-fit model to match the $\lesssim$0.5 day luminosity, as shown by the brown curves (1.05 $M_\odot$ WD + 0.0111 $M_\odot$ He shell), demonstrating the high sensitivity of model predictions to the He-shell mass. However, this model provides a worse fit to the subsequent light curves during 0.5–5 days, the timing and duration of the early color evolution (left panels), and near-peak observations (see Section 7.3 below) of SN 2018aoz than the magenta model. The implications of these discrepancies are discussed in Section 8.5 below.

7.3. Comparison to Maximum-light Properties

Figure 13 compares the near-peak spectrum of SN 2018aoz with that of the He-shell DDet models. All of the models predict clear absorption features in the vicinity of the observed Si II, S II, Fe II/III, and Ca II features in SN 2018aoz, as labeled at the top of the left panel. The models with 1.05 $M_\odot$ WD mass provide the best match to the observed spectral features.

Figure 14 (top panel; adapted from Polin et al. 2019, Figure 11) compares both the peak luminosity and ejecta velocity, measured by the peak B-band magnitude and Si II velocity, of SN 2018aoz to those of the He-shell DDet models along with other Type Ia SNe and previously published He-shell DDet models from Polin et al. (2019). The cyan and red models provide the best matches to the observed peak B-band magnitude and ejecta velocity of SN 2018aoz (orange star), respectively, while the magenta model with a 1.05 $M_\odot$ WD + 0.010 $M_\odot$ He shell provides the closest match when both features are simultaneously considered. However, we note that there is some separation between SN 2018aoz and the models. In particular, Polin et al. (2019) identified two broad populations of SNe within this plot: an apparent clustering at $v_{\rm peak}$ (Si II) $\sim$11,000 km s^{-1} and high peak magnitudes, and a non-clustered population with a tail extending to higher velocities. The former is mainly composed of CN and 91T-like Type Ia SNe, while the latter is composed of BL and 91bg-like events (see Figure B1, bottom panel). As noted by Polin et al. (2019), the He-shell DDet models exhibit a peak brightness and velocity relationship (black-dashed line) that generally follows the BL/91bg-like tail. Several key predicted features of He-shell DDet are also prevalent among SNe from

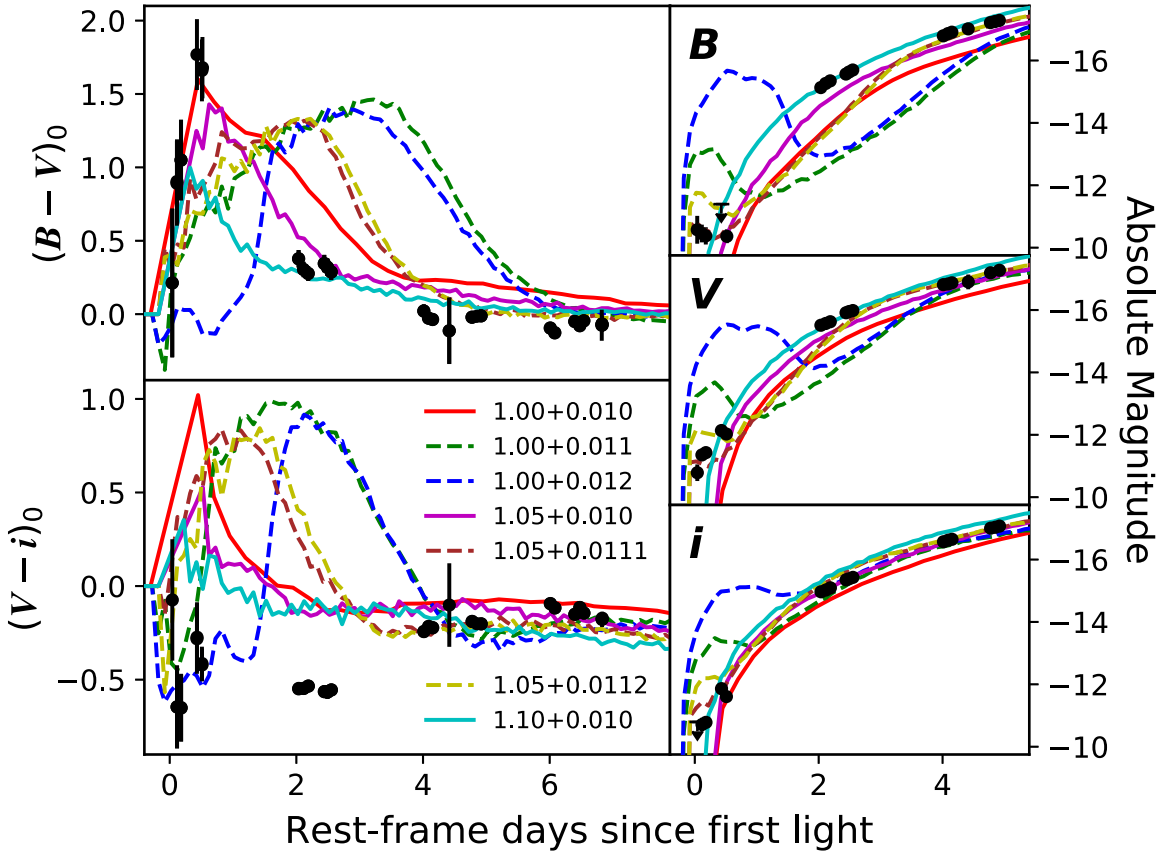

Figure 12. The early observations of SN 2018aoz (black circles), including the dereddened color (left panels) and light (right panels) curves in the rest frame, are compared to the outcomes of the He-shell DDet simulations (colored curves) labeled with WD mass + He-shell mass in $M_\odot$. The inverted arrow (top-right) is a detection limit at an S/N of 2.

the BL/91bg-like tail, including sub-Chandrasekhar inferred ejecta masses (Scalzo et al. 2019) and lack of C spectral features (Maguire et al. 2014), consistent with a He-shell DDet origin for them (Polin et al. 2019). For SN 2018aoz, the measured values of M_B (peak) $= -19.319 \pm 0.009$ mag and $v_{\rm peak}$ (Si II) $= (11.43 \pm 0.12) \times 10^3$ km s^{-1} place it close to the boundary between the CN/91T-like cluster and the BL/91bg-like tail populations, consistent with its intermediate nature between CN and BL (Section 3.3), though it is more similar to events from the CN/91T-like cluster overall.

While SN 2018aoz could simply be an edge case between these two populations, in some other maximum-light features there is even less agreement between SN 2018aoz and the He-shell DDet models. In Figure 14 (middle panel), we add SN 2018aoz to Figure 12 from Polin et al. (2019), which plots the peak B-band magnitude, Si II velocity, and $B-V$ *color*, $B_{\rm max}-V_{\rm max}$, for a population of Type Ia SNe (circles) and He-shell DDet models (squares). Polin et al. (2019) noted that most objects from the BL/91bg-like tail population in this plot of the peak B-band magnitude versus peak Si II velocity exhibit red $B_{\rm max}-V_{\rm max}$ consistent with the models, further suggesting a common He-shell DDet origin. In contrast, SN 2018aoz with a relatively blue $B_{\rm max}-V_{\rm max}$ of -0.093 ± 0.013 is more consistent with the clustered CN events.

7.4. Comparison to Nebular-phase Properties

The nebular-phase flux ratio of the 7290 Å emission feature to [Fe III] λ4658 Å, (7290 Å/[Fe III]; Section 6.2) from ~120–320 days since the peak has also been suggested to distinguish He-shell DDet events from other normal Type Ia SNe (Polin et al. 2021). He-shell DDet models typically produce substantially more Ca than what is predicted in Chandrasekhar-mass explosions as a result of incomplete nuclear burning in the core of sub-Chandrasekhar-mass WDs, which may be observed as strong [Ca II] emission near 7290 Å in the optically thin nebular phase (Section 6.4). In the bottom panel of Figure 14 (adapted from Polin et al. 2021, Figure 9), we compare SN 2018aoz to the same population of Type Ia SNe and set of He-shell DDet models as in the top panel with the color scale now representing their nebular-phase 7290 Å/[Fe III] ratios. As noted by Polin et al. (2021), SNe from the BL/91bg-like tail show stronger contributions from [Ca II], leading to larger 7290 Å/[Fe III] ratios consistent with the He-shell DDet model predictions, while those from the CN/91T-like cluster have smaller ratios. For SN 2018aoz, its relatively small 7290 Å/[Fe III] ratio of 0.149 ± 0.007 once again identifies it with the SNe from the CN-subtype cluster, which are inconsistent with the He-shell DDet models.

7.5. Search for Carbon

Another key prediction of He-shell DDet models is efficient carbon burning, which leaves $\lesssim 10^{-5}\,M_\odot$ of unburnt carbon in the SN ejecta (Polin et al. 2019) in contrast to the substantial amount ($\sim$0.03 $M_\odot$) typically predicted by some other explosion models such as pure deflagration (Nomoto et al. 1984) and pulsating delayed detonation (Hoflich et al. 1995). We search for the C II λ6580 Å absorption feature near Si II λ6355 Å that has been used to examine the presence of carbon in Type Ia SN

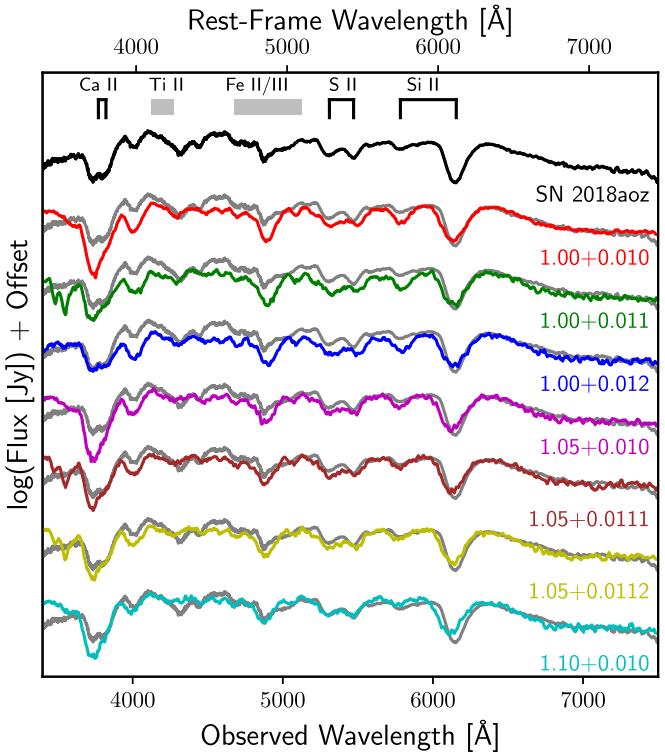

Figure 13. The dereddened spectrum of SN 2018aoz (black and gray curves) from 1.9 days before the *B*-band maximum in the rest frame (∼13.9 days since explosion) is compared to the outcomes of the same-colored He-shell DDet simulations of Figure 12 from the nearest post-explosion phase for various WD and He-shell masses as labeled (WD mass + He-shell mass in $M_\odot$). For a clear comparison, the simulated spectra have been smoothed by boxcar convolution, resulting in effective spectral resolutions of $R = 300$.

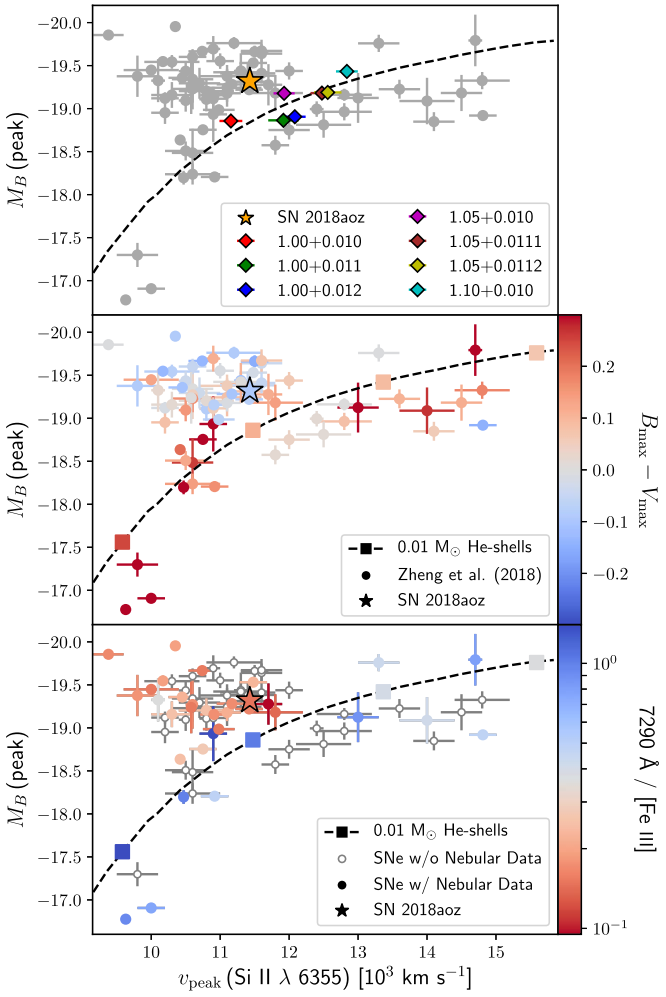

Figure 14. The distribution of M_B (peak) vs. v_{peak} (Si II) of SN 2018aoz (filled stars) and the outcomes of our He-shell DDet simulations (filled diamonds with the same colors as the models from Figures 12 and 13) compared with that of other SNe (circles) and He-shell DDet models from (Polin et al. 2019, top and middle panels) and (Polin et al. 2021, bottom panel), where M_B (peak) and v_{peak} (Si II) represent the peak *B*-band absolute magnitude and Si II velocity, respectively. (Note that the two parameters of the other SNe used in Polin et al. 2019, 2021 are originally from Zheng et al. 2018.) The dashed curves represent the relationship between the two parameters predicted by the He-shell DDet models (filled squares in the middle and bottom panels) of Polin et al. (2019) with 0.01 $M_\odot$ He shells. The colors of the data points in the middle panel correspond to $B_{max}-V_{max}$ magnitudes (right-hand *y*-axis), while those of the filled data points in the bottom panel correspond to the nebular-phase 7290 Å/[Fe III] line ratio. The SNe with large $B_{max}-V_{max}$ magnitudes (red-colored circles in the middle panel) and large 7290 Å/[Fe III] ratios (blue-colored circles in the bottom panel) scattered near the dashed lines have been suggested to be produced by He-shell DDets (Polin et al. 2019, 2021).

ejecta (Parrent et al. 2011; Blondin et al. 2012; Maguire et al. 2014). As detailed below, although C II λ6580 Å is expected to be visible if the carbon mass fraction in the photosphere is greater than ∼0.005 (Heringer et al. 2019), we detect no such feature in SN 2018aoz throughout its evolution. This indicates that the carbon mass fraction is below this value in most layers of the ejecta of SN 2018aoz, compatible with the He-shell DDet prediction. We note, however, that the absence of unburnt carbon is also possible for some non-DDet explosion models (e.g., pulsating delayed detonations with very slow deflagration speeds; Hoflich et al. 1995).

Figure 15 compares the predicted spectral evolution (magenta curves) of the best-fit He-shell DDet model (1.05 $M_\odot$ WD + 0.010 $M_\odot$ He shell) to the observed spectra of SN 2018aoz until approximately the *B*-band maximum. We find an absence of the C II λ6580 Å feature in all the spectra starting from as early as 4.4 days since the first light (−11.0 days since the *B*-band maximum), consistent with a lack of unburnt carbon throughout most layers of the ejecta. However, the lack of earlier spectroscopic observations before 4.4 days of probing carbon in the fast-expanding outer ejecta potentially allows a substantial amount of unburnt carbon to be hidden in the outer ∼30% of the ejected mass (Equation (2)). Note also that C II in Type Ia SNe has been detected as early as −15 days since the *B*-band maximum (Parrent et al. 2011), earlier than our first spectroscopic observations. In some cases, the C II feature fades to become undetectable long before the *B*-band maximum (Brown et al. 2019); however, in NUV-blue events (e.g., SN 2011fe; Pereira et al. 2013), the C II λ6580 Å feature is almost always visible until roughly the *B*-band maximum (see Milne et al. 2013, and references therein). Since SN 2018aoz is an extremely NUV-blue event (Section 3.2), the absence of C II from −11 days since the *B*-band maximum in the source appears to be an exceptional case.

8. The Nature of SN 2018aoz and Implications for the Origins of Type Ia SNe

8.1. Nature of the Companion Star

Our analyses of the early light curves (Section 4) and nebular-phase spectra (Section 6.3) of SN 2018aoz indicate that the binary companion of its progenitor is most likely a

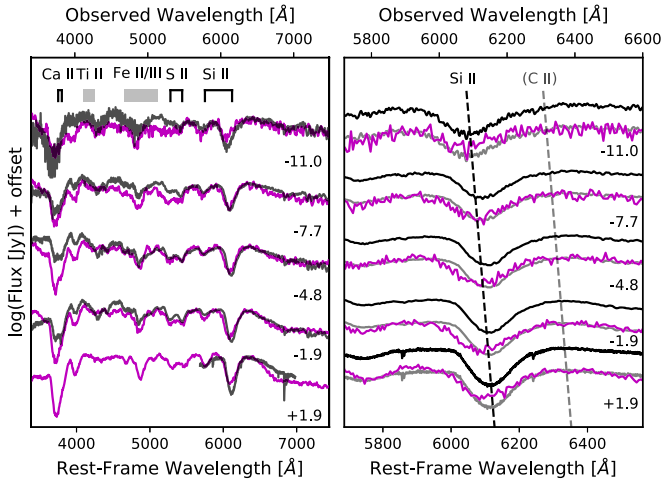

Figure 15. (Left) The dereddened early spectra of SN 2018aoz (black) are compared to the predictions of the best-fit He-shell DDet model (1.05 $M_\odot$ WD + 0.010 $M_\odot$ He shell; magenta curves) in the rest frame, as labeled in days since the *B*-band maximum. For a clear comparison, the model spectra have been filtered by boxcar convolution, resulting in effective spectral resolutions of $R = 300$. (Right) Same as the left panel, but showing unfiltered model spectra zoomed in on the vicinity of the observed Si II absorption feature. The observed (black) spectra are translated downward (gray) by subtracting a constant value for better comparison with the best-fit He-shell DDet model predictions (magenta). The approximate minima of the observed Si II features and the expected relative positions of the C II absorption feature are shown with black- and gray-dashed lines, respectively. Note that C II is not visible in any of the spectra.

secondary WD. First, our analysis of the early light curves disfavors binary companions larger than low-mass (a few solar mass) main-sequence stars based on the absence of their ejecta-companion interaction emission, leaving low-mass main-sequence stars at large viewing angles ($\gtrsim 80°$) naked He stars, and WDs as the most likely possibilities for the companion. Note that all three possibilities have been predicted to be involved in Type Ia SN explosions (Maoz et al. 2014). Second, our modeling of the nebular-phase spectra of SN 2018aoz further disfavors low-mass main-sequence stars and naked He stars as follows. In the single-degenerate scenario, the SN ejecta is expected to strip/ablate ~0.1–0.5 $M_\odot$ of H-/He-rich material from the companion (Dessart et al. 2020), and most models predict that this leads to H emission in the nebular phase (Mattila et al. 2005; Botyanszki et al. 2018; Dessart et al. 2020) while one model also predicts He emission (Botyanszki et al. 2018). Our modeling of the nebular-phase spectra permits $\lesssim 10^{-2}\,M_\odot$ of each element, disfavoring the single-degenerate scenario for SN 2018aoz, consistent with what has been found in 94% of Type Ia SNe (Tucker et al. 2020). We note, however, that disagreements between current model predictions for the emission from early ejecta-companion interactions (Kasen 2010; Kutsuna & Shigeyama 2015) and from stripped/ablated materials in the nebular phase (Botyanszki et al. 2018; Dessart et al. 2020) preclude a definitive determination of the companion nature based on these analyses for now.

Although we cannot rule out a single-degenerate progenitor for SN 2018aoz, we can almost completely rule out the case for an RG companion, as predicted in the classical single-degenerate scenario. Such a companion likely requires an extreme viewing angle in order to hide the ejecta-companion interaction in the early phase and emission from stripped/ablated H in the nebular phase, as supported by multiple models (Mattila et al. 2005; Kasen 2010; Kutsuna & Shigeyama 2015; Botyanszki et al. 2018; Dessart et al. 2020). The He-star channel for Type Ia SNe is also a less favorable progenitor for SN 2018aoz due to the short ($\lesssim$0.2 Gyr) delay time of the channel after star formation (Wang & Han 2010). This delay time is difficult to reconcile with the immediate environment of the SN due to the lack of recent star formation therein. Metal abundance ratios $\gtrsim 40''$ from the center of NGC 3923 reflect an old (~8–14 Gyr) stellar age in those regions (Kim et al. 2012), while recent star formation in the halo of NGC 3923 where SN 2018aoz was found is even less feasible. The lack of recent star formation at the SN location is also supported by the lack of local dust extinction (Sakurai et al. 2013), as evidenced by the absence of Na I doublet lines at the host galaxy redshift (Paper I).

8.2. Origin of the Infant-phase Excess Emission

We have shown that three mechanisms are capable of producing the observed infant-phase excess emission in SN 2018aoz (Section 5): (1) radioactive heating by surface Fe-peak elements; (2) ejecta interaction with the binary companion; or (3) ejecta interaction with CSM. Since the presence of surface Fe-peak elements is also required to explain the observed *B*-band suppression, it is likely that at least *some* of the emission is due to radioactive heating by those same Fe-peak elements. However, the luminosity produced will depend sensitively on both the specific nucleosynthetic products in the outer ejecta (which will vary with the explosion mechanism) as well as the degree of gamma-ray trapping. Indeed, as shown in Section 7.2, it is possible for physical models to produce the level of *B*-band suppression needed to explain the NRB, while underpredicting the infant-phase luminosity. Thus, ejecta interactions with the binary companion and/or CSM may also contribute to—and potentially dominate—the luminosity at early times.

Within this context, we note that both the ejecta-companion and ejecta-CSM interaction cases for the origin of the infant-phase excess emission in SN 2018aoz are compatible with its favored double-degenerate progenitor (Section 8.1). In the case of ejecta-companion interaction, the observed infant-phase excess emission requires a small binary companion size, consistent with either a WD, He star, or low-mass (a few solar mass) main-sequence star (Section 5.2).

In the case of an ejecta-CSM interaction, CSM with a small mass and radius is required, consistent with what is expected from the companion accretion process (Section 5.3). The mass of CSM needed for the observed infant-phase excess emission ($\gtrsim 10^{-3}\,M_\odot$) and our strongest constraints on swept-up H from the nebular-phase spectra ($\lesssim 4 \times 10^{-4}\,M_\odot$; Table 6) further requires the fractional mass of H in the total CSM mass to be $\lesssim$50%. These mass requirements are compatible with H-poor CSM originating from the accretion process of either a WD or He-star companion.

8.3. Explosion Geometry and Progenitor Mass

As noted in Paper I and Section 7, the relatively short 15.3 days rise time of SN 2018aoz indicates that SN 2018aoz was either (1) a spherically symmetric explosion with a low total ejecta mass of ~0.8–1.0; or (2) an asymmetric explosion. The weak strength of [Ca II] emission in the nebular phase of SN 2018aoz disfavors the former (Section 6.4). However, in

the remaining case of a high ejecta mass asymmetric explosion, the extreme blueshifts of the observed nebular-phase [Fe II] and [Ni II] features in SN 2018aoz conflict with the observation of a short rise time (Section 6.4).

We examine three possible scenarios that can explain the weak [Ca II] emission and blueshifts of [Fe II] and [Ni II] emission in the nebular-phase 7290 Å feature of SN 2018aoz simultaneously with its short rise time.

1. SN 2018aoz may originate from the explosion of a relatively high-mass ($\gtrsim$1.2 $M_\odot$) WD, where complete nuclear burning in the core results in weak nebular-phase [Ca II] emission. The explosion can be moderately asymmetric, resulting in blueshifted [Fe II] and [Ni II] lines in the nebular phase from a viewing angle where the ejecta core is approaching the observer. In this case, the fast-rising light curves of SN 2018aoz can only be explained by the presence of a preceding dark phase (Piro & Nakar 2013). However, this scenario is disfavored for two reasons. First, we found no evidence of a long (>1 day) dark phase in SN 2018aoz (Paper I) based on its observed ejecta velocity evolution (Piro & Nakar 2014). Second, for an asymmetric Chandrasekhar-mass explosion, such a viewing angle would be less compatible with the presence of surface Fe-peak elements, which is primarily predicted in the direction where the ejecta core is receding from the observer (e.g., Maeda et al. 2010a).
2. Alternatively, the explosion of a high-mass WD could be compatible with the fast-rising light curve if the ejecta core is receding from the observer. In this case, blueshifted [Fe II] and [Ni II] lines in the nebular phase may require them to be optically thick, causing the shielding of the receding part of the ejecta by the approaching part. Note that Fe-peak elements have been suggested to act as a Fe *curtain*, blocking the radiation from obstructed regions (Leonard 2007; Dessart et al. 2020).
3. SN 2018aoz may originate from the asymmetric explosion of a lower-mass WD. Since nuclear burning is more complete in the densest regions of the ejecta, which is near the off-center point of carbon ignition, Ca production increases toward the low-density opposing direction (e.g., Boos et al. 2021). For a highly asymmetric explosion, there could be limited overlap between the distributions of Ca- and Fe-peak elements in the core, resulting in weak [Ca II] emission in the nebular phase (Hoeflich et al. 2021; Polin et al. 2021). For a moderately asymmetric explosion where the core is approaching the observer, shielding of the most Ca-rich regions by parts of the intervening core may cause blueshifted [Fe II] and [Ni II] to dominate the 7290 Å feature if their lines are optically thick.

8.4. Implications for the Asymmetric Chandrasekhar-mass Explosion Mechanism

One possible origin of surface Fe-peak elements associated with the observed *B*-band suppression in SN 2018aoz is subsonic mixing in an asymmetric Chandrasekhar-mass explosion (Paper I), which has long been theorized to produce normal Type Ia SNe and their observed properties. In particular, the relationship between the observed light curves of Type Ia SNe and $\Delta M_{15}(B)$ (i.e., Phillips relation; Phillips et al. 1999), as well as the residual differences in their peak luminosities, peak colors, and nebular-phase [Fe II] and [Ni II] line shifts, have been found to be attributable to viewing angle effects and the details of the deflagration-to-detonation transition in the model (Kasen et al. 2009; Maeda et al. 2010c, 2010b, 2011). A Chandrasekhar-mass explosion is also the main scenario that is thought to produce Type Ia SNe with weak [Ca II] emission in the nebular phase (Mazzali et al. 2015; Polin et al. 2021), such as SN 2018aoz, since complete nuclear burning in the core of high-mass WDs produces little Ca. However, as explained in Sections 6.4 and 8.3, both the short rise time and presence of surface Fe-peak elements in SN 2018aoz point to a viewing angle where the ejecta core is receding from the observer under the asymmetric Chandrasekhar-mass explosion scenario. Reconciling the receding motion of the ejecta core with the observed blueshifts of nebular-phase [Fe II] and [Ni II] in SN 2018aoz may thus require those lines to remain optically thick until ~380 days post-peak.

Between low-mass (a few solar mass) main-sequence and WD companions for the progenitor system of SN 2018aoz (Section 8.1), the former is more compatible with the standard Chandrasekhar-mass explosion model, though it would require modifications to models that predict material will be stripped/ablated from the companion and visible at late times (Botyanszki et al. 2018; Dessart et al. 2020). In contrast, if the companion is a WD, then this scenario faces a number of constraints due to the accretion process between WDs often being dynamically unstable (Shen 2015) and tending to result in either a He-shell DDet or a violent merger. The former (=He-shell DDet) leads to a different explosion mechanism as discussed below (Section 8.5), while the latter (=violent merger) is disfavored by the absence of unburnt O and He signatures in the nebular phase (Section 6.3). To avoid dynamically evolving toward He-shell DDet or violent merger, the case of a Chandrasekhar-mass explosion for SN 2018aoz under double degeneracy may require a relatively massive and rare primary WD that is already near the Chandrasekhar mass (~1.4 $M_\odot$) at the start of accretion, significantly larger than that of most WDs in the range of 0.5–0.8 $M_\odot$(Tremblay et al. 2016). Alternatively, a violent merger is still possible if the nebular-phase O and He emission lines are hidden by metal line-blanket absorption. In this case, the observed infant-phase excess emission would need to be from surface radioactive heating since a premerger explosion is required for both (1) ejecta-companion interactions to occur and (2) ejecta-CSM interaction properties to be compatible with the infant-phase observations (Section 5.3).

8.5. Implications for the He-shell DDet Explosion Mechanism

He-shell DDet is another explosion mechanism that naturally explains the presence of surface Fe-peak elements associated with the observed *B*-band suppression in SN 2018aoz (Paper I). 1D simulations of thin He-shell DDets (Section 7) are able to reproduce the rapid $B-V$ color evolution of the NRB phase in SN 2018aoz, as well as its overall spectroscopic features and light curves, with the 1.05 $M_\odot$ WD + 0.010 $M_\odot$ model providing the best fit. Thus, a He-shell DDet origin for SN 2018aoz would confirm the predictions of recent theoretical models indicating that detonations of He shells as thin as 0.01 $M_\odot$ can successfully trigger Type Ia SNe, including normal events. In addition to the presence of surface Fe-peak

elements, SN 2018aoz also exhibits a number of other features that may be explained by a He-shell DDet origin. This includes (1) the absence of C spectral features (Section 7.5), (2) the short observed rise time, which can be explained by a sub-Chandrasekhar ejecta mass (Paper I), and (3) the small inferred companion size (Section 8.1), as the typical progenitor channels for He-shell DDets involve accretion from a He-star, He-WD, or He/CO hybrid companion (Guillochon et al. 2010; Shen & Bildsten 2014).

However, SN 2018aoz fails several additional diagnostic criteria proposed by Polin et al. (2019, 2021) that are used to recognize this explosion mechanism. First, the current suite of He-shell DDet models cannot entirely reproduce the infant-phase features of SN 2018aoz (Section 7.2). The 1.05 $M_\odot$ WD + 0.010 $M_\odot$ He-shell model is the only He-shell DDet model that can match the early ($\lesssim$5 days since the first light) $B-V$ color evolution of SN 2018aoz associated with surface Fe-peak elements; however, this model underpredicts the observed luminosity of the infant-phase excess emission and produces early ($\lesssim$4 days) $V-i$ colors that are redder than observed. Second, although SN 2018aoz exhibits properties in common with both CN and BL subtypes of Type Ia SNe (Section 3.3), its blue near-peak color appears to be more compatible overall with the bulk of CN events as opposed to the swath of BL (and also 91bg-like) events that show reddened near-peak colors predicted to be caused by ashes of the He-shell detonation (Section 7.3). Third, compared to the He-shell DDet models of Polin et al. (2021) and other Type Ia SNe, the nebular-phase 7290 Å/[Fe III] flux ratio observed in SN 2018aoz is much lower than what is predicted in the models as well as what is observed in the BL/91bg-like events suspected to be from He-shell DDet (Section 7.4).

Thus, the observed properties of SN 2018aoz appear less compatible with the model predictions overall and show a closer resemblance to SNe that are not suspected of being thin He-shell DDets than SNe that are. This disfavors the He-shell DDet explosion mechanism for the origin of SN 2018aoz, or at least requires modifications to the standard scenario of thin He-shell DDets as described by Polin et al. (2019, 2021). The first two discrepancies may be attributable to differences in the ashes of the initial He-shell detonation between the models and SN 2018aoz, which would impact both the radioactive heating rate in the infant phase and spectroscopic features near the maximum light (Magee et al. 2021). Different nucleosynthetic yields may be possible if the evolutionary path leads to a He shell with different initial conditions (e.g., composition, density) from those adopted by the models. The under-prediction of early luminosity by the best-fit He-shell DDet model may also indicate that an additional source of luminosity beyond radioactive heating is required at early times (e.g., shock interaction).

In contrast, the production of nebular-phase [Ca II] emission in sub-Chandrasekhar-mass explosions primarily depends on the total mass of the progenitor WD and the relative distribution of Ca and radioactive Fe-peak elements in the ejecta core. Recent multidimensional He-shell DDet simulations have found that the explosion mechanism is inherently nonspherically symmetric (e.g., Boos et al. 2021), and its viewing angle effects have been suggested to explain the different ejecta velocities of Type Ia SNe from the CN and BL subtypes as well as their differences in peak colors and nebular-phase [Fe II] line shifts (Li et al. 2019; Boos et al. 2021). The asymmetric explosion can also shift the distributions of Ca and Fe-peak elements. As noted in Section 8.3, nuclear burning in an asymmetric sub-Chandrasekhar-mass explosion is more complete near the ignition point of the central carbon, which results in the distribution of Ca being offset toward the opposite side of the ejecta core. Thus, a viewing angle where the Ca-rich region is shielded by the core may result in [Ca II] being hidden if the [Fe II] and [Ni II] lines remain optically thick in the nebular phase. Weak [Ca II] emission may also result from a sub-Chandrasekhar-mass explosion with a higher total mass (e.g., 1.26 $M_\odot$; Mazzali et al. 2015). However, as with the case of a Chandrasekhar-mass explosion (Section 8.4), reconciling the short rise time of SN 2018aoz with the high ejecta mass in this case may still require optically thick [Fe II] and [Ni II] lines. More detailed multidimensional modeling is necessary to ascertain if such effects can explain the observations of SN 2018aoz.

8.6. The D∧6 Scenario

One specific He-shell DDet scenario that may yield initial conditions varying from the hydrostatic models of Polin et al. (2019, 2021) and also arises from the favored double-degenerate progenitor of SN 2018aoz is a D∧6 (Shen et al. 2018), scenario. D∧6 is a proposed origin for Type Ia SNe wherein dynamic (unstable) accretion during the coalescence of a double-degenerate binary composed of two WDs leads to a Type Ia SN triggered by He-shell DDet. While detailed models would be necessary to assess the overall consistency of D∧6 with observations of SN 2018aoz, motivated by the possible requirement of additional emission sources beyond radioactive heating at early times (Section 8.5), we show below that D∧6 also naturally provides infant-phase emission at the level observed in SN 2018aoz via ejecta interactions with CSM and/or the companion.

First, due to the dynamic nature of the accretion, a torus of CSM is expected to be present around the primary WD at the time of explosion (e.g., Guillochon et al. 2010; Pakmor et al. 2013). As detailed in Section 5.3, the small mass and radius ($\lesssim$0.007 $M_\odot$ and $\lesssim 10^{10}$ cm) of CSM required to fit the observed infant-phase excess emission is compatible with CSM properties predicted in hydrodynamic simulations of this accretion process. Note that the fitted CSM properties were obtained by assuming an ejecta mass of 1.05 $M_\odot$, which is favored by He-shell DDet models (Section 7.1).

Second, models have shown that when all nuclear reactions are considered (Shen & Moore 2014) the He-shell DDet of the primary can occur during the early phases of dynamical accretion, before the companion WD has been fully disrupted (Pakmor et al. 2013). Thus, for the D ∧ 6 scenario, ejecta interaction with the companion should occur. Dynamically unstable mass transfer between two WDs is expected for mass ratios $\gtrsim$0.2 (Shen et al. 2018), corresponding to companion masses of $\gtrsim$0.2 $M_\odot$ for a 1.05 $M_\odot$ primary. Adopting the temperature of $\sim 3.0 \times 10^4$ K for a tidally heated He WD in Roche overflow and the corresponding mass–radius relationship (Panei et al. 2007), the expected separation for a 0.2 $M_\odot$ He WD is $\sim 1.2 \times 10^{10}$ cm while larger companion masses lead to smaller separation distances. These separations overlap with the lower end of the binary separation distances (6.8×10^9 cm; Section 5.2) that can fit the observed infant-phase excess emission for an assumed ejecta mass of 1.05 $M_\odot$. In addition, rapid mass loss during dynamical accretion is expected to both

widen the binary and inflate the donor WD (Kremer et al. 2015), indicating that both higher mass He WDs and He/CO hybrids could also provide non-negligible contribution to the infant-phase excess emission of SN 2018aoz in the D∧6 scenario.

We note that if either ejecta-companion or ejecta-CSM interaction is the origin of the observed infant-phase excess emission under D∧6, two distinct physical processes would be required to produce the infant-phase features of SN 2018aoz: line-blanket absorption by surface Fe-peak elements produced in the He-shell DDet; and shock interaction from the ejecta colliding with either the companion or CSM. While these processes are naturally predicted together in the D∧6 scenario at the low-luminosity level probed by the infant-phase observations of SN 2018aoz, we emphasize that there are currently no theoretical models that consider the observational outcomes of both processes simultaneously.

8.7. Implications for the Explosion Mechanisms of Normal Type Ia SNe

The exact explosion mechanism of SN 2018aoz remains uncertain—as neither asymmetric Chandrasekhar-mass explosion nor He-shell DDet models are currently capable of explaining all of the observations. However, whatever its nature, the explosion mechanism of SN 2018aoz appears to produce a Type Ia SN with normal properties after the infant phase, indicating that it is a potentially prevalent explosion mechanism among Type Ia SNe. As shown in Section 3.3, SN 2018aoz is intermediate between the CN and BL subtypes of normal Type Ia SNe—corresponding to 38% and 30% of the entire Type Ia SN population (Blondin et al. 2012), respectively—and shares spectroscopic similarities with both groups. Thus, assuming that the reported infant-phase features first identified in SN 2018aoz are found among spectroscopically similar SNe, then an explosion mechanism capable of producing normal Type Ia SNe with surface Fe-peak elements may be responsible for up to 68% of Type Ia SNe from these two normal subtypes.

9. Summary and Conclusion

The observations of SN 2018aoz starting from the infant phase (<1 day since the first light) and continuing to the late nebular phase (≳200 days since the peak) have provided one of the most extensive sets of clues for understanding the origin and evolution of a Type Ia SN. We summarize our main results and conclusions as follows.

1. The near-peak light curves and spectroscopic features of SN 2018aoz show that it is intermediate between the CN/NV and BL/HV subtypes of normal Type Ia SNe, manifesting its nature as a normal event. The evolution of its $B-V$ and $V-i$ colors after the infant phase are also consistent with those of other normal Type Ia SNe, while the infant-phase color evolution is revealed for the first time, showing the rapid reddening of both colors over the first ∼0.5 day (or NRB). SN 2018aoz belongs to the NUV-blue group of normal Type Ia SNe based on its UV-optical colors, with some of the bluest UV-optical colors reported in the group prior to the *B*-band maximum. No C spectral features are detected throughout the SN evolution beginning from the first spectrum ∼4.4 days since the first light, which is exceptional among NUV-blue events while similar to typical BL events.
2. The early *BVi*-band light curves of SN 2018aoz during 0–7 days consist of three components wherein two infant-phase features are embedded in an underlying power-law component that rises overall during the period. The two infant-phase features are the (1) *B*-band plateau during ∼0–1 day (Paper I) and (2) excess emission during 0.08–0.42 day, together resulting in the NRB color evolution.
3. The *B*-band plateau feature has been attributed to *B*-band suppression by surface Fe-peak elements (Paper I), while we find that three mechanisms can contribute to the observed infant-phase excess emission: (1) radioactive heating by the surface Fe-peak elements; (2) ejecta shock interaction with the binary companion; and (3) ejecta shock interaction with CSM.
4. Shock breakout is unlikely to be a significant contributor to the infant-phase excess emission.
5. A small companion—such as a WD, He star, or low-mass (a few solar mass) main-sequence star—is required to attribute the infant-phase excess emission to ejecta-companion interaction, and the absence of H and He emission lines throughout the nebular phase favors the WD companion. The presence of an RG companion is particularly incompatible with the observed luminosity over the first few days, while the environment of the SN in the halo of the NGC 3923 elliptical galaxy argues against short delay-time companions, including He stars as well as high-mass giants.
6. Attributing the infant-phase excess emission to ejecta-CSM interaction requires a CSM distribution with a small total mass ($\lesssim 0.007\,M_{\odot}$) and radius ($\lesssim 10^{10}$ cm) at the time of explosion, more consistent with what is expected during the binary accretion process than after a violent merger. The presence of CSM from a violent merger is further disfavored by the absence of He and O lines in the nebular phase.
7. The weak strength of nebular-phase [Ca II] emission and the observed blueshifts of [Fe II] and [Ni II] are not well explained by either explosions of high- or low-mass WDs. Both cases may require [Fe II] and [Ni II] lines to remain optically thick until ∼380 days since the peak in addition to explosion asymmetry.
8. Our 1D thin He-shell DDet simulations are capable of explaining the observed $B-V$ NRB color evolution associated with the *B*-band suppression by surface Fe-peak elements, overall evolution of optical luminosity and spectra, and absence of C spectral features in SN 2018aoz. However, the model that best matches the observed $B-V$ color evolution of the SN fails to reproduce its infant-phase excess emission and early $V-i$ color. In addition, in a number of observed properties that have been suggested to identify the explosion mechanism, including $B_{\rm max}-V_{\rm max}$ and nebular-phase [Ca II]/[Fe III] line ratio, SN 2018aoz is more similar to the bulk of CN Type Ia SNe, as opposed to the population of BL/91bg-like SNe that closely resemble the He-shell DDet models. Modifications to the standard thin He-shell DDet scenario (e.g., explosion asymmetry) may ameliorate some of these discrepancies.

9. Both asymmetric Chandrasekhar-mass explosion and the D∧6 scenario accommodate the presence of surface Fe-peak elements and the observed infant-phase excess emission in SN 2018aoz. However, neither model is currently capable of explaining all of the observations.
10. The normal Type Ia nature of SN 2018aoz and its spectroscopic similarity with a significant fraction of the Type Ia SN population indicates that SN 2018aoz shares a common origin with at least some fraction of normal events, assuming that the reported infant-phase features first identified in SN 2018aoz are found among spectroscopically similar SNe.

Our analyses highlight the importance of (1) deep, high-cadence survey observations that are capable of probing the low-luminosity signals of Type Ia SNe in their earliest phases and (2) follow-up observations of light curves and spectra over the entire evolution of the SN until the nebular phase. As the only Type Ia SN to date with sufficiently early (=∼0–0.5 day) and deep (=∼ −10 to −12 absolute *AB* magnitudes) multi-band observations to detect the infant-phase *B*-band suppression and excess emission, SN 2018aoz can provide an important point of reference for future efforts to model crucial physical processes in the infancy of Type Ia SN explosions.

This research has made use of the KMTNet system operated by the Korea Astronomy and Space Science Institute (KASI) and the data were obtained at three host sites of CTIO in Chile, SAAO in South Africa, and SSO in Australia. This research is also based on observations obtained at the international Gemini-S Observatory, a program of NSF's NOIRLab, which is managed by the Association of Universities for Research in Astronomy (AURA) under a cooperative agreement with the National Science Foundation on behalf of the Gemini Observatory partnership: the National Science Foundation (United States), National Research Council (Canada), Agencia Nacional de Investigación y Desarrollo (Chile), Ministerio de Ciencia, Tecnología e Innovación (Argentina), Ministério da Ciência, Tecnologia, Inovações e Comunicações (Brazil), and Korea Astronomy and Space Science Institute (Republic of Korea). The Gemini-S observations were obtained under the K-GMT Science Program (PID: GS-2018A-Q-117 and GS-2018B-Q-121) of KASI and acquired through the Gemini Observatory Archive at NSF's NOIRLab. This paper includes data gathered with the 6.5 m Magellan Telescopes located at Las Campanas Observatory, Chile. This work makes use of observations from the Las Cumbres Observatory (LCO) global telescope network. The LCO team is supported by NSF grants AST-1911225 and AST-1911151, and NASA Swift grant 80NSSC19K1639. The Swift observations were triggered through the Swift GI program 80NSSC19K0316. SOUSA is supported by NASA's Astrophysics Data Analysis Program through grant NNX13AF35G. Some of the data presented herein were obtained at the W. M. Keck Observatory, which is operated as a scientific partnership among the California Institute of Technology, the University of California, and the National Aeronautics and Space Administration. The Observatory was made possible by the generous financial support of the W. M. Keck Foundation. The Computational HEP program in The Department of Energy's Science Office of High Energy Physics provided simulation resources through grant #KA2401022. This research used resources of the National Energy Research Scientific Computing Center, a U.S. Department of Energy Office of Science User Facility operated under Contract No. DE-AC02-05CH11231. D.-S.M., M.R.D., and C.D.M. are supported by Discovery Grants from the Natural Sciences and Engineering Research Council of Canada. D.-S.M. was supported in part by a Leading Edge Fund from the Canadian Foundation for Innovation (project No. 30951). M.R.D. was supported in part by the Canada Research Chairs Program, the Canadian Institute for Advanced Research (CIFAR), and the Dunlap Institute at the University of Toronto. D.J.S. acknowledges support by NSF grants AST-1821987, 1821967, 1908972 and from the Heising-Simons Foundation under grant No. 2020-1864. S.G.-G. acknowledges support by FCT under Project CRISP PTDC/FIS-AST-31546 and Project UIDB/00099/2020. S.C.K., Y.L., and H.S.P. acknowledge support by KASI under the R&D program (Project No. 2022-1-868-04) supervised by the Ministry of Science and ICT. H.S.P. was supported in part by the National Research Foundation of Korea (NRF) grant funded by the Korean government (MSIT, Ministry of Science and ICT; No. NRF-2019R1F1A1058228). P.J.B. acknowledges support from the Swift GI program 80NSSC19K0316. S.V., Y.D., and K.A.B. acknowledge support by NSF grants AST-1813176 and AST-2008108. C. M. acknowledges support by NSF grant AST-1313484. R.L.B. acknowledges support by NASA through Hubble Fellowship grant No. 51386.01 awarded by the Space Telescope Science Institute, which is operated by the Association of Universities for Research in Astronomy, Inc., for NASA, under contract NAS 5-26555. A.G.-Y's research is supported by the EU via ERC grant No. 725161, the ISF GW excellence center, an IMOS space infrastructure grant and BSF/Transformative and GIF grants, as well as the André Deloro Institute for Advanced Research in Space and Optics, the Schwartz/Reisman Collaborative Science Program and the Norman E. Alexander Family M Foundation ULTRASAT Data Center Fund, Minerva and Yeda-Sela; A.G.-Y. is the incumbent of The Arlyn Imberman Professorial Chair. L.G. acknowledges financial support from the Spanish Ministerio de Ciencia e Innovación (MCIN), the Agencia Estatal de Investigación (AEI) 10.13039/501100011033, and the European Social Fund (ESF) "Investing in your future" under the 2019 Ramón y Cajal program RYC2019-027683-I and the PID2020-115253GA-I00 HOSTFLOWS project, and from Centro Superior de Investigaciones Científicas (CSIC) under the PIE project 20215AT016. G.P. acknowledges support by ANID—Millennium Science Initiative—ICN12_009 and by FONDECYT Regular 1201793. J.A. is supported by the Stavros Niarchos Foundation (SNF) and the Hellenic Foundation for Research and Innovation (H.F.R.I.) under the 2nd Call of "Science and Society" Action Always strive for excellence—"Theodoros Papazoglou" (project No. 01431).

Software: SNooPy (Burns et al. 2011), Castro (Almgren et al. 2010; Zingale et al. 2018), Sedona (Kasen et al. 2006), SNAP (https://github.com/niyuanqi/SNAP), IRAF.

Appendix A
Optical Color Evolution After the Infant Phase

The color evolution of SN 2018aoz after the infant phase is characterized by phase transitions at −4.6, 10.4, and 26.0 days since the *B*-band maximum, marked by the second, third, and fourth vertical dotted lines in Figure 4, respectively. These epochs are roughly aligned with the primary peak, the onset of the secondary rise, and the secondary peak of the *i*-band light

curve. These mark four clear phases of Type Ia SN color evolution first described by Moon et al. (2021).

1. Between the first and second color transition epochs, during the *i*-band primary rise, the $B-V$ color of SN 2018aoz evolves blueward by 0.4 mag while the $V-i$ color evolves redward by 0.4 mag before both colors become stalled prior to the second color transition epoch. The blueward $B-V$ color evolution during this phase is consistent with that of the *early-red* group of Type Ia SNe (Stritzinger et al. 2018), dominated by normal events. During this phase, the $B-V$ color is thought to evolve blueward as a result of increased heating from ^{56}Ni within the ejecta as it is revealed by the SN expansion (Piro & Nakar 2014; Hoeflich et al. 2017). While SNe have rarely been observed with $V-i$ color in such early epochs, the redward $V-i$ color evolution of SN 2018aoz during this phase appears similar to those of SN 2004D (Patat et al. 1996) and KSP-OT-201509b (Moon et al. 2021), two normal Type Ia SNe from the over- and subluminous extremes, respectively, attributed to the evolution of spectral features in the *i* bands (Moon et al. 2021), e.g., Ca II (Parrent et al. 2012, see Figure 1 therein).
2. By the second color transition epoch, near the *i*-band primary peak, both $B-V$ and $V-i$ colors have reversed their direction of evolution, evolving redward and blueward, respectively. The redward $B-V$ color evolution has been attributed to the development of Fe-peak absorption features in the *B* band and the blueward $V-i$ color evolution to the continued temperature increase as deeper deposits of ^{56}Ni within the ejecta continue to be exposed by the SN expansion (Moon et al. 2021).
3. While the $B-V$ color sustains redward evolution by 1.0 mag until the fourth color transition epoch, the $V-i$ color, after evolving blueward by 1.0 mag, changes direction again at the third color transition epoch, coinciding with the onset of the secondary rise in the *i* band. The *i*-band secondary rise, which is due to the increased line opacity in the *B* and *V* bands from the recombination of Fe III (Kasen 2006), causes the $V-i$ color to evolve redward by 1.2 mag until the fourth color transition epoch.
4. After the fourth color transition epoch, near the *i*-band secondary peak, both $B-V$ and $V-i$ colors evolve linearly blueward at rates of 0.013 and 0.009 mag day^{-1}, respectively, as the SN enters the *Lira law phase* ($\gtrsim$30 days post-peak). During this phase, the intrinsic $B-V$ colors of Type Ia SNe evolve blueward linearly, following the Lira law (Phillips et al. 1999).

The dotted line in Figure 4 (top panel) represents the Lira law evolution of the $B-V$ color of Type Ia SNe from Burns et al. (2014), which provides a Lira law slope of -0.011 mag day^{-1} for $s_{BV}=0.797$. The difference of $\sim$0.003 mag day^{-1} between the observed $B-V$ slope of SN 2018aoz in the Lira law phase and that of the Lira law is consistent with the observed range of scatter in the $B-V$ slopes of Type Ia SNe in the Lira law phase ($\sim$0.004 mag day^{-1}; Burns et al. 2014). Thus, we find that a simple vertical shift corresponding to a reddening of $E(B-V)=0.09$ mag, assuming $R_V=3.1$, is sufficient to match the Lira law to the observed color evolution of SN 2018aoz. This reddening is consistent with the Galactic extinction expected toward the direction of the source, supporting a negligible amount of extragalactic extinction for SN 2018aoz as expected from its location in the halo of NGC 3923.

Appendix B
Light-curve Classification

The classification of SN 2018aoz as a normal Type Ia SN that is intermediate between the CN and BL subtypes (Section 3.3) is supported by its near-peak light curves as follows. Figure B1 (top panel) compares the peak *B*-band absolute magnitude and $\Delta M_{15}(B)$ light-curve parameters of SN 2018aoz to those of other Type Ia SNe from the CN, BL, 91bg-like, and 91T-like subtypes. The parameters of SN 2018aoz are consistent with both CN and BL subtypes of the normal Type Ia SNe, while they are inconsistent with the subluminous/fast-declining 91bg-like and the overluminous/slow-declining 91T-like events. This confirms that SN 2018aoz is normal, belonging to either CN or BL, though the two subtypes are not clearly distinguished based on their light-curve properties alone. The bottom panel compares the peak Si II velocity and $\Delta M_{15}(B)$ of SN 2018aoz with those of other Type Ia SNe from the same four subtypes as in the top panel. As seen in the panel, the CN and BL subtypes are more easily separated by these two parameters. The Si II velocity and $\Delta M_{15}(B)$ of SN 2018aoz are each consistent with both CN and BL subtypes, while the SN itself is located within the CN-subtype cluster. This confirms that SN 2018aoz exhibits properties in

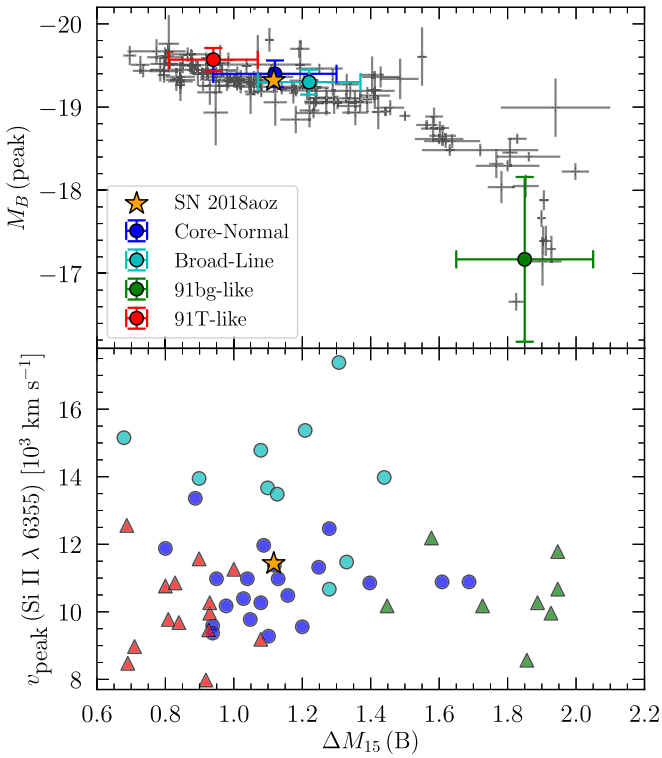

Figure B1. (Top) Comparison of $\Delta M_{15}(B)$ and M_B of SN 2018aoz (orange star; Paper I) measured in the rest frame with those of other Type Ia SNe (gray crosses, Burns et al. 2018). The colored circles represent the average values for the four main subtypes of Type Ia SNe (Parrent et al. 2014): CN (blue), BL (cyan), 91bg-like (green), and 91T-like (red). (Bottom) Comparison of $\Delta M_{15}(B)$ and the peak Si II velocity of SN 2018aoz (orange star) with those of other Type Ia SNe (colored circles; Parrent et al. 2014). The colors represent the same subtypes of Type Ia SNe as in the top panel.

common with both CN and BL subtypes, consistent with its intermediate classification, though the SN may be more similar to CN/NV than BL/HV events overall.

We note that for a normal Type Ia SN, the pre-peak light curves of SN 2018aoz rise exceptionally fast. Population studies of Type Ia SNe find rise times of 18–25 days from the first light to the *B*-band maximum in normal events by fitting power-laws with indices of 2 to the early light curves (Riess et al. 1999; Aldering et al. 2000; Conley et al. 2006), while rise times of 15–22 days are found when the power-law index is freely fitted (Miller et al. 2020b). The 15.32 day rise time of SN 2018aoz, measured using a power-law fit with a free index (Ni et al. 2022), is consistent with what has been found in normal events, but near the low end of the distribution.

Appendix C
Effect of Infant-phase *B*-band Suppression on Companion Constraints

In our analyses in Section 4, we excluded the *B*-band light curve of SN 2018aoz during 0–1 day since the first light from the comparisons between the observed brightness and the model prediction from ejecta-companion interactions. Figure B2 is the same as Figure 9, but obtained by comparing the entire *BVri* early light curves of SN 2018aoz during 0–3 days, including those of the *B*-band plateau (top-left panel). The inclusion of the *B*-band plateau results in much stronger constraints on the companion by disallowing separation distances from $\sim 10^{11}$ to $\sim 4 \times 10^{13}$ cm for almost all viewing angles (Figure B2, right panel). This substantially increases the likelihood of small companions (i.e., WD or He star) for SN 2018aoz, with main-sequence and subgiant companions of $>1\,M_{\odot}$ now essentially excluded and those with smaller masses (i.e., M or K dwarfs) only allowed for a more limited range of viewing angles of $\sim 90°$–$180°$. These clearly show that, compared to the *Vri* bands, the early *B*-band light curve of SN 2018aoz over-constrains its companion to favor much smaller ones as a result of being suppressed by surface Fe-peak elements (Paper I). Our results suggest that caution needs to be exercised in general when future observations probing the infant-phase evolution of Type Ia SNe are used to constrain physical parameters of progenitors and explosion mechanisms, such as the companion size based on comparing the model brightness and light curves.

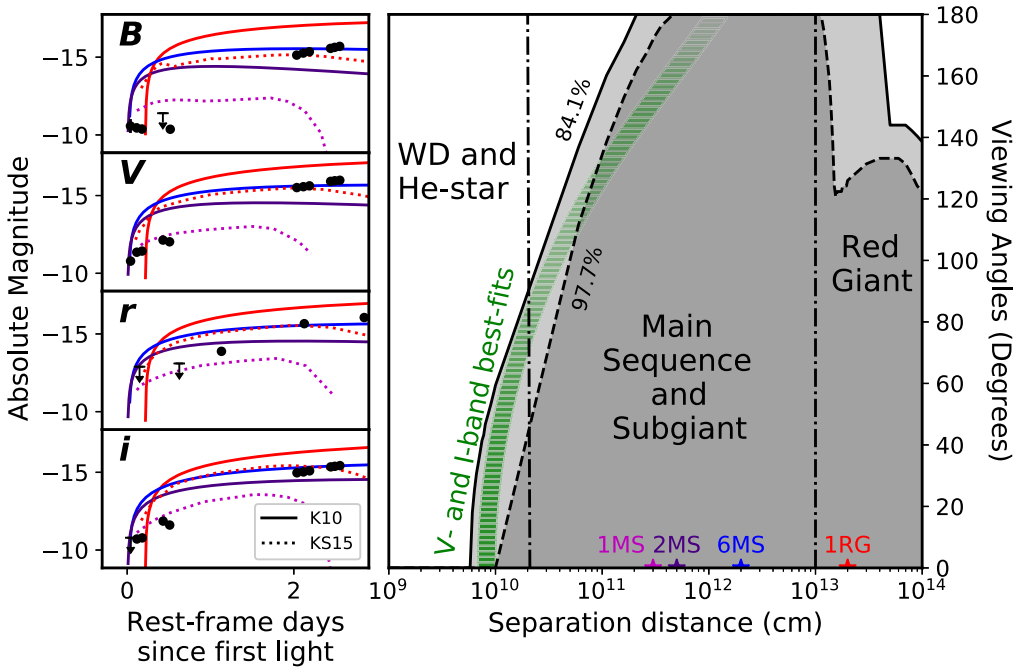

Figure B2. (Left) Same as Figure 9, but including the *B*-band light curve (top). (Right) Same as Figure 9, but the solid and dashed lines representing the 84.1% and 97.7% confidence levels are calculated for the full *BVri*-band light curves, including that of the infant-phase *B*-band plateau, which is affected by *B*-band suppression.

ORCID iDs

Yuan Qi Ni https://orcid.org/0000-0003-3656-5268
Dae-Sik Moon https://orcid.org/0000-0003-4200-5064
Maria R. Drout https://orcid.org/0000-0001-7081-0082
Abigail Polin https://orcid.org/0000-0002-1633-6495
David J. Sand https://orcid.org/0000-0003-4102-380X
Santiago González-Gaitán https://orcid.org/0000-0001-9541-0317
Sang Chul Kim https://orcid.org/0000-0001-9670-1546
Youngdae Lee https://orcid.org/0000-0002-6261-1531
Hong Soo Park https://orcid.org/0000-0002-3505-3036
D. Andrew Howell https://orcid.org/0000-0003-4253-656X
Peter E. Nugent https://orcid.org/0000-0002-3389-0586
Anthony L. Piro https://orcid.org/0000-0001-6806-0673
Peter J. Brown https://orcid.org/0000-0001-6272-5507
Lluís Galbany https://orcid.org/0000-0002-1296-6887
Jamison Burke https://orcid.org/0000-0003-0035-6659
Daichi Hiramatsu https://orcid.org/0000-0002-1125-9187
Griffin Hosseinzadeh https://orcid.org/0000-0002-0832-2974
Stefano Valenti https://orcid.org/0000-0001-8818-0795
Niloufar Afsariardchi https://orcid.org/0000-0002-1338-490X
Jennifer E. Andrews https://orcid.org/0000-0003-0123-0062
John Antoniadis https://orcid.org/0000-0003-4453-3776
Rachael L. Beaton https://orcid.org/0000-0002-1691-8217
K. Azalee Bostroem https://orcid.org/0000-0002-4924-444X
Raymond G. Carlberg https://orcid.org/0000-0002-7667-0081
S. Bradley Cenko https://orcid.org/0000-0003-1673-970X
Sang-Mok Cha https://orcid.org/0000-0002-7511-2950
Yize Dong https://orcid.org/0000-0002-7937-6371
Avishay Gal-Yam https://orcid.org/0000-0002-3653-5598
Joshua Haislip https://orcid.org/0000-0002-6703-805X
Thomas W.-S. Holoien https://orcid.org/0000-0001-9206-3460
Sean D. Johnson https://orcid.org/0000-0001-9487-8583
Vladimir Kouprianov https://orcid.org/0000-0003-3642-5484
Yongseok Lee https://orcid.org/0000-0001-7594-8072
Christopher D. Matzner https://orcid.org/0000-0001-9732-2281
Nidia Morrell https://orcid.org/0000-0003-2535-3091
Curtis McCully https://orcid.org/0000-0001-5807-7893
Giuliano Pignata https://orcid.org/0000-0003-0006-0188
Daniel E. Reichart https://orcid.org/0000-0002-5060-3673
Jeffrey Rich https://orcid.org/0000-0002-5807-5078
Stuart D. Ryder https://orcid.org/0000-0003-4501-8100
Nathan Smith https://orcid.org/0000-0001-5510-2424
Samuel Wyatt https://orcid.org/0000-0003-2732-4956
Sheng Yang https://orcid.org/0000-0002-2898-6532

References

Afsariardchi, N., & Matzner, C. D. 2018, ApJ, 856, 146
Afsariardchi, N., Moon, D.-S., Drout, M. R., et al. 2019, ApJ, 881, 22
Aldering, G., Knop, R., & Nugent, P. 2000, AJ, 119, 2110
Allington-Smith, J., Breare, M., Ellis, R., et al. 1994, PASP, 106, 983
Almgren, A. S., Beckner, V. E., Bell, J. B., et al. 2010, ApJ, 715, 1221
Arnett, W. D. 1982, ApJ, 253, 785
Ashall, C., Lu, J., Shappee, B. J., et al. 2022, ApJL, 932, L2
Aznar-Siguan, G., Garcia-Berro, E., Loren-Aguilar, P., Soker, N., & Kashi, A. 2015, MNRAS, 450, 2948
Bauer, E. B., Chandra, V., Shen, K. J., & Hermes, J. J. 2021, ApJL, 923, L34
Benetti, S., Cappellaro, E., Mazzali, P. A., et al. 2005, ApJ, 623, 1011
Blondin, S., Matheson, T., Kirshner, R. P., et al. 2012, AJ, 143, 126
Bloom, J. S., Kasen, D., Shen, K. J., et al. 2012, ApJL, 744, L17
Boos, S. J., Townsley, D. M., Shen, K. J., Caldwell, S., & Miles, B. J. 2021, ApJ, 919, 126
Botyanszki, J., Kasen, D., & Plewa, T. 2018, ApJL, 852, L6
Branch, D., Dang, L., Hall, N., et al. 2006, PASP, 118, 560
Branch, D., Lacy, C. H., McCall, M. L., et al. 1983, ApJ, 270, 123
Brown, P., & Sand, D. 2018, ATel, 11511, 1
Brown, P. J., Dawson, K. S., de Pasquale, M., et al. 2012, ApJ, 753, 22
Brown, P. J., Hosseinzadeh, G., Jha, S. W., et al. 2019, ApJ, 877, 152
Brown, P. J., Kuin, P., Scalzo, R., et al. 2014, ApJ, 787, 29
Brown, P. J., Landez, N. J., Milne, P. A., & Stritzinger, M. D. 2017, ApJ, 836, 232
Brown, T. M., Baliber, N., Bianco, F. B., et al. 2013, PASP, 125, 1031
Bulla, M., Miller, A. A., Yao, Y., et al. 2020, ApJ, 902, 48
Burns, C. R., Stritzinger, M., Phillips, M. M., et al. 2011, AJ, 141, 19
Burns, C. R., Stritzinger, M., Phillips, M. M., et al. 2014, ApJ, 789, 32
Burns, C. R., Parent, E., Phillips, M. M., et al. 2018, ApJ, 869, 56
Cartier, R., Sullivan, M., Firth, R. E., et al. 2017, MNRAS, 464, 4476
Conley, A., Howell, D. A., Howes, A., et al. 2006, AJ, 132, 1707
Dan, M., Rosswog, S., Bruggen, M., & Podsiadlowski, P. 2014, MNRAS, 438, 14
De, K., Kasliwal, M. M., Polin, A., et al. 2019, ApJL, 873, L18
Deckers, M., Maguire, K., Magee, M. R., et al. 2022, MNRAS, 512, 1317
Dessart, L., Leonard, D. C., & Prieto, J. L. 2020, A&A, 638, A80
Dimitriadis, G., Foley, R. J., Rest, A., et al. 2019, ApJL, 870, L1
Drout, M. R., Milisavljevic, D., Parrent, J., et al. 2016, ApJ, 821, 57
Flörs, A., Spyromilio, J., Taubenberger, S., et al. 2020, MNRAS, 491, 2902
Foley, R. J., Challis, P. J., Filippenko, A. V., et al. 2012, ApJ, 744, 38
Guillochon, J., Dan, M., Ramirez-Ruiz, E., & Rosswog, S. 2010, ApJL, 709, L64
Heringer, E., Kerkwijk, M. H. v., Sim, S. A., Kerzendorf, W. E., & Graham, M. L. 2019, ApJ, 871, 250
Hoflich, P., Khokhlov, A. M., & Wheeler, J. C. 1995, ApJ, 444, 831
Hoeflich, P., Ashall, C., Bose, S., et al. 2021, ApJ, 922, 186
Hoeflich, P., Hsiao, E. Y., Ashall, C., et al. 2017, ApJ, 846, 58
Holmbo, S., Stritzinger, M. D., Shappee, B. J., et al. 2019, A&A, 627, A174
Hook, I. M., Jørgensen, I., Allington-Smith, J. R., et al. 2004, PASP, 116, 425
Hosseinzadeh, G., Sand, D. J., Lundqvist, P., et al. 2022, ApJL, 933, L45
Hosseinzadeh, G., Sand, D. J., Valenti, S., et al. 2017, ApJL, 845, L11
Hosseinzadeh, G., Valenti, S., Sand, D., et al. 2018, Transient Name Server Classification Report, No. 2018-433
Iben, I., Jr., & Tutukov, A. V. 1984, ApJS, 54, 335
Iben, I., Jr., & Tutukov, A. V. 1994, ApJ, 431, 264
Iben, I. J., Tutukov, A. V., & Fedorova, A. V. 1998, ApJ, 503, 344
Jiang, J.-A., Doi, M., Maeda, K., & Shigeyama, T. 2018, ApJ, 865, 149
Jiang, J.-A., Doi, M., Maeda, K., et al. 2017, Natur, 550, 80
Kasen, D. 2006, ApJ, 649, 939
Kasen, D. 2010, ApJ, 708, 1025
Kasen, D., Ropke, F. K., & Woosley, S. E. 2009, Natur, 460, 869
Kasen, D., Thomas, R. C., & Nugent, P. 2006, ApJ, 651, 366
Katz, B., Budnik, R., & Waxman, E. 2010, ApJ, 716, 781
Kim, D.-W., Fabbiano, G., & Pipino, A. 2012, ApJ, 751, 38
Kim, S.-L., Lee, C.-U., Park, B.-G., et al. 2016, JKAS, 49, 37
Kirshner, R. P., Jeffery, D. J., Leibundgut, B., et al. 1993, ApJ, 415, 589
Kollmeier, J. A., Chen, P., Dong, S., et al. 2019, MNRAS, 486, 3041
Kremer, K., Sepinsky, J., & Kalogera, V. 2015, ApJ, 806, 76
Kromer, M., Pakmor, R., Taubenberger, S., et al. 2013, ApJL, 778, L18
Kromer, M., Sim, S. A., Fink, M., et al. 2010, ApJ, 719, 1067
Kuchner, M. J., Kirshner, R. P., Pinto, P. A., & Leibundgut, B. 1994, ApJL, 426, L89
Kushnir, D., Katz, B., Dong, S., Livne, E., & Fernandez, R. 2013, ApJL, 778, L37
Kutsuna, M., & Shigeyama, T. 2015, PASJ, 67, 54
Lee, Y., Kim, S. C., Moon, D.-S., et al. 2022, ApJL, 925, L22
Leonard, D. C. 2007, ApJ, 670, 1275
Li, W., Wang, X., Bulla, M., et al. 2021, ApJ, 906, 99
Li, W., Wang, X., Vinko, J., et al. 2019, ApJ, 870, 12
Maeda, K., Benetti, S., Stritzinger, M., et al. 2010c, Natur, 466, 82
Maeda, K., Jiang, J.-A., Shigeyama, T., & Doi, M. 2018, ApJ, 861, 78
Maeda, K., Röpke, F. K., Fink, M., et al. 2010a, ApJ, 712, 624
Maeda, K., Taubenberger, S., Sollerman, J., et al. 2010b, ApJ, 708, 1703

Maeda, K., Leloudas, G., Taubenberger, S., et al. 2011, MNRAS, 413, 3075
Magee, M. R., Maguire, K., Kotak, R., & Sim, S. A. 2021, MNRAS, 502, 3533
Maguire, K., Sim, S. A., Shingles, L., et al. 2018, MNRAS, 477, 3567
Maguire, K., Sullivan, M., Pan, Y. C., et al. 2014, MNRAS, 444, 3258
Maguire, K., Taubenberger, S., Sullivan, M., & Mazzali, P. A. 2016, MNRAS, 457, 3254
Maoz, D., Mannucci, F., & Nelemans, G. 2014, ARA&A, 52, 107
Marion, G. H., Brown, P. J., Vinko, J., et al. 2016, ApJ, 820, 92
Matheson, T., Kirshner, R. P., Challis, P., et al. 2008, AJ, 135, 1598
Mattila, S., Lundqvist, P., Sollerman, J., et al. 2005, A&A, 443, 649
Mazzali, P. A., Benetti, S., Stritzinger, M., & Ashall, C. 2022, MNRAS, 511, 5560
Mazzali, P. A., Ropke, F. K., Benetti, S., & Hillebrandt, W. 2007, Sci, 315, 825
Mazzali, P. A., Sullivan, M., Filippenko, A. V., et al. 2015, MNRAS, 450, 2631
Meikle, W. P. S., Cumming, R. J., Geballe, T. R., et al. 1996, MNRAS, 281, 263
Meng, X., & Li, J. 2019, MNRAS, 482, 5651
Miller, A. A., Cao, Y., Piro, A. L., et al. 2018, ApJ, 852, 100
Miller, A. A., Magee, M. R., Polin, A., et al. 2020a, ApJ, 898, 56
Miller, A. A., Yao, Y., Bulla, M., et al. 2020b, ApJ, 902, 47
Milne, P. A., Brown, P. J., Roming, P. W. A., Bufano, F., & Gehrels, N. 2013, ApJ, 779, 23
Moffat, A. F. J. 1969, A&A, 3, 455
Moon, D.-S., Kim, S. C., Lee, J.-J., et al. 2016, Proc. SPIE, 9906, 99064I
Moon, D.-S., Ni, Y. Q., Drout, M. R., et al. 2021, ApJ, 910, 151
Munari, U., Henden, A., Belligoli, R., et al. 2013, NewA, 20, 30
Nakar, E., & Piro, A. L. 2014, ApJ, 788, 193
Nakar, E., & Sari, R. 2010, ApJ, 725, 904
Ni, Y. Q. 2022, SuperNova Analysis Package (SNAP) ver221207, Zenodo, doi:10.5281/zenodo.7411663
Ni, Y. Q., Moon, D.-S., Drout, M. R., et al. 2022, NatAs, 6, 568
Nomoto, K., Thielemann, F. K., & Yokoi, K. 1984, ApJ, 286, 644
Nugent, P. E., Sullivan, M., Cenko, S. B., et al. 2011, Natur, 480, 344
Oke, J. B., Cohen, J. G., Carr, M., et al. 1995, PASP, 107, 375
Olling, R. P., Mushotzky, R., Shaya, E. J., et al. 2015, Natur, 521, 332
Pakmor, R., Kromer, M., Taubenberger, S., et al. 2012, ApJL, 747, L10
Pakmor, R., Kromer, M., Taubenberger, S., & Springel, V. 2013, ApJL, 770, L8
Panei, J. A., Althaus, L. G., Chen, X., & Han, Z. 2007, MNRAS, 382, 779
Park, H. S., Moon, D.-S., Zaritsky, D., et al. 2017, ApJ, 848, 19
Parrent, J., Friesen, B., & Parthasarathy, M. 2014, Ap&SS, 351, 1
Parrent, J. T., Howell, D. A., Friesen, B., et al. 2012, ApJL, 752, L26
Parrent, J. T., Thomas, R. C., Fesen, R. A., et al. 2011, ApJ, 732, 30
Patat, F., Benetti, S., Cappellaro, E., et al. 1996, MNRAS, 278, 111
Pereira, R., Thomas, R. C., Aldering, G., et al. 2013, A&A, 554, A27
Perley, D. A. 2019, PASP, 131, 084503
Perlmutter, S., Aldering, G., Goldhaber, G., et al. 1999, ApJ, 517, 565
Phillips, M. M., Lira, P., Suntzeff, N. B., et al. 1999, AJ, 118, 1766
Pignata, G., Benetti, S., Mazzali, P. A., et al. 2008, MNRAS, 388, 971
Piro, A. L. 2015, ApJL, 808, L51
Piro, A. L., Chang, P., & Weinberg, N. N. 2010, ApJ, 708, 598
Piro, A. L., & Morozova, V. S. 2016, ApJ, 826, 96
Piro, A. L., & Nakar, E. 2013, ApJ, 769, 67
Piro, A. L., & Nakar, E. 2014, ApJ, 784, 85
Polin, A., Nugent, P., & Kasen, D. 2019, ApJ, 873, 84
Polin, A., Nugent, P., & Kasen, D. 2021, ApJ, 906, 65
Reinecke, M., Hillebrandt, W., & Niemeyer, J. C. 2002, A&A, 391, 1167
Riess, A. G., Filippenko, A. V., Challis, P., et al. 1998, AJ, 116, 1009
Riess, A. G., Filippenko, A. V., Li, W., et al. 1999, AJ, 118, 2675
Sakurai, A., Takeuchi, T. T., Yuan, F. T., Buat, V., & Burgarella, D. 2013, EP&S, 65, 203
Sand, D., Valenti, S., Wyatt, S., et al. 2018a, ATel, 11496, 1
Sand, D. J., Amaro, R. C., Moe, M., et al. 2019, ApJL, 877, L4
Sand, D. J., Graham, M. L., Botyánszki, J., et al. 2018b, ApJ, 863, 24
Scalzo, R. A., Parent, E., Burns, C., et al. 2019, MNRAS, 483, 628
Schwab, J., Shen, K. J., Quataert, E., Dan, M., & Rosswog, S. 2012, MNRAS, 427, 190
Seeds, M. A. 1984, Foundations of Astronomy (Belmont, CA: Wadsworth Pub. Co.)
Shappee, B. J., Piro, A. L., Stanek, K. Z., et al. 2018, ApJ, 855, 6
Shappee, B. J., Stanek, K. Z., Pogge, R. W., & Garnavich, P. M. 2013, ApJL, 762, L5
Shen, K. J. 2015, ApJL, 805, L6
Shappee, B. J., Holoien, T. W. S., Drout, M. R., et al. 2019, ApJ, 870, 13
Shen, K. J., & Bildsten, L. 2014, ApJ, 785, 61
Shen, K. J., Blondin, S., Kasen, D., et al. 2021a, ApJL, 909, L18
Shen, K. J., Boos, S. J., Townsley, D. M., & Kasen, D. 2021b, ApJ, 922, 68
Shen, K. J., Boubert, D., Gansicke, B. T., et al. 2018, ApJ, 865, 15
Shen, K. J., & Moore, K. 2014, ApJ, 797, 46
Siebert, M. R., Dimitriadis, G., Polin, A., & Foley, R. J. 2020, ApJL, 900, L27
Stritzinger, M., Hamuy, M., Suntzeff, N. B., et al. 2002, AJ, 124, 2100
Stritzinger, M. D., Shappee, B. J., Piro, A. L., et al. 2018, ApJL, 864, L35
Tartaglia, L., Sand, D. J., Valenti, S., et al. 2018, ApJ, 853, 62
Taubenberger, S., Kromer, M., Pakmor, R., et al. 2013, ApJL, 775, L43
Townsley, D. M., Miles, B. J., Shen, K. J., & Kasen, D. 2019, ApJL, 878, L38
Tremblay, P. E., Cummings, J., Kalirai, J. S., et al. 2016, MNRAS, 461, 2100
Trujillo, I., Aguerri, J. A. L., Cepa, J., & Gutiérrez, C. M. 2001, MNRAS, 328, 977
Tsvetkov, D. Y., Shugarov, S. Y., Volkov, I. M., et al. 2013, CoSka, 43, 94
Tucker, M. A., Ashall, C., Shappee, B. J., et al. 2022, ApJL, 926, L25
Tucker, M. A., Ashall, C., Shappee, B. J., et al. 2021, ApJ, 914, 50
Tucker, M. A., Shappee, B. J., Vallely, P. J., et al. 2020, MNRAS, 493, 1044
von Boetticher, A., Triaud, A. H. M. J., Queloz, D., et al. 2017, A&A, 604, L6
Wang, B., & Han, Z. 2010, A&A, 515, A88
Wang, X., Filippenko, A. V., Ganeshalingam, M., et al. 2009, ApJL, 699, L139
Wang, X., Wang, L., Filippenko, A. V., Zhang, T., & Zhao, X. 2013, Sci, 340, 170
Weaver, T. A. 1976, ApJS, 32, 233
Whelan, J., & Iben, I. J. 1973, ApJ, 186, 1007
Woosley, S. E., & Kasen, D. 2011, ApJ, 734, 38
Yao, Y., Miller, A. A., Kulkarni, S. R., et al. 2019, ApJ, 886, 152
Zhang, K. D., Murakami, Y. S., Stahl, B. E., Patra, K. C., & Filippenko, A. V. 2021, MNRAS Lett., 503, L33
Zheng, W., Kelly, P. L., & Filippenko, A. V. 2018, ApJ, 858, 104
Zingale, M., Almgren, A. S., Barrios Sazo, M. G., et al. 2018, JPhCS, 1031, 012024